nature communications

Article

https://doi.org/10.1038/s41467-024-51236-6

Sculpting the tumour microenvironment by combining radiotherapy and ATR inhibition for curative-intent adjuvant immunotherapy

Received: 5 January 2024

Accepted: 19 July 2024

Published online: 13 August 2024

Check for updates

Emmanuel C. Patin[1] ✉, Pablo Nenclares[1,2], Charleen Chan Wah Hak[1,2], Magnus T. Dillon[1,2], Anton Patrikeev[1], Martin McLaughlin[1], Lorna Grove[1,2], Shane Foo[1], Heba Soliman[2], Joao P. Barata[2], Joanna Marsden[2], Holly Baldock[1], Jim Gkantalis[1], Victoria Roulstone[1], Joan Kyula[1], Amy Burley[1], Lisa Hubbard[1], Malin Pedersen[1], Simon A. Smith[3], Eleanor Clancy-Thompson[3], Alan A. Melcher[4], Masahiro Ono[5], Antonio Rullan[1,2] & Kevin J. Harrington[1,2]

The combination of radiotherapy/chemoradiotherapy and immune checkpoint blockade can result in poor outcomes in patients with locally advanced head and neck squamous cell carcinoma (HNSCC). Here, we show that combining ATR inhibition (ATRi) with radiotherapy (RT) increases the frequency of activated NKG2A$^+$PD-1$^+$ T cells in animal models of HNSCC. Compared with the ATRi/RT treatment regimen alone, the addition of simultaneous NKG2A and PD-L1 blockade to ATRi/RT, in the adjuvant, post-radiotherapy setting induces a robust antitumour response driven by higher infiltration and activation of cytotoxic T cells in the tumour microenvironment. The efficacy of this combination relies on CD40/CD40L costimulation and infiltration of activated, proliferating memory CD8$^+$ and CD4$^+$ T cells with persistent or new T cell receptor (TCR) signalling, respectively. We also observe increased richness in the TCR repertoire and emergence of numerous and large TCR clonotypes that cluster based on antigen specificity in response to NKG2A/PD-L1/ATRi/RT. Collectively, our data point towards potential combination approaches for the treatment of HNSCC.

New treatment modalities are urgently needed to reduce the number of patients that relapse after multimodality treatment for locally advanced head and neck squamous cell carcinoma (HNSCC). To achieve this goal, we must improve our understanding of strategies that seek to combine radiotherapy, chemotherapy, targeted therapy and/or immunotherapy (ImmuT). Immune checkpoint blockade (ICB) has significant activity as a single-agent and in combination with chemotherapy in recurrent/metastatic HNSCC[1–3], irrespective of human papillomavirus (HPV) status. However, concomitant addition of ICB has so far shown no evidence of improving standard-of-care radiotherapy/chemoradiotherapy for locally advanced HNSCC[4,5] (NCT03040999). Since simple addition of concomitant anti-PD1/-PD-L1 blocking antibodies to radiotherapy/chemoradiotherapy fails to improve outcomes, alternative approaches involving combinations with antibodies targeting other immune checkpoints, including anti-NKG2A, are under preclinical and clinical development.

The inhibitory receptor NKG2A is a member of the C-type lectin superfamily expressed on both T and NK cells[6]. Downstream inhibitory

[1]Targeted Therapy Team, The Institute of Cancer Research, London, UK. [2]The Royal Marsden Hospital, London, UK. [3]Early Oncology R&D, AstraZeneca, Cambridge, UK. [4]Translational Immunotherapy Team, The Institute of Cancer Research, London, UK. [5]Department of Life Sciences, Imperial College London, London, UK. ✉e-mail: emmanuel.patin@icr.ac.uk

signalling via NKG2A relies on the recruitment of SHP-1/2 phosphatases which subsequently suppress the activity of activating receptors such as NKG2D. Preclinical data indicated that anti-NKG2A synergised with anti-PD-1/PD-L1 by boosting the activity of NK and CD8 T cells[7]. NKG2A inhibition also delayed tumour growth after peptide vaccination in various mouse tumour models[8]. In clinical studies, the humanised anti-NKG2A antibody monalizumab, in combination with durvalumab, showed manageable toxicities and promising activity in patients with microsatellite-stable colorectal cancer[9]. The same combination, tested in the COAST and NeoCOAST studies, increased therapeutic benefits when compared to durvalumab alone in non-small-cell lung cancer[10,11]. In the context of HNSCC, monalizumab alone did not significantly improve therapeutic outcome in the UPSTREAM clinical trial[12]. Nevertheless, evaluation of monalizumab, in combination with durvalumab, is under investigation in the same trial. The recent failure of the INTERLINK-1 clinical trial (NCT04590963) of monalizumab and cetuximab in recurrent and/or metastatic HNSCC has refocused efforts on combinations of monalizumab with anti-PD1/-PD-L1 agents.

Another strategy to augment the efficacy of ICB is through combination with RT and radiosensitizers, such as DNA damage response inhibitors (DDRi). One such DDRi, the ATR inhibitor (ATRi), ceralasertib, has been under clinical investigations for head and neck cancer[13]. We and others previously reported that ATRi could potentiate RT-mediated antitumour immunity, creating a favourable tumour microenvironment (TME) for ICB interventions[14–16]. Indeed, combining ATRi/RT with anti-PD-L1 blockade significantly improved tumour growth control and survival in mice[17,18]. Additionally, our group also recently described how dual anti-PD-1/-TIGIT blockade could enhance NK-cell-mediated tumour control after ATRi/RT[15]. Following those preclinical studies, combination of ATRi, RT and ICB is now entering clinical trials for the treatment of HNSCC (NCT04576091 and EudraCT 2020-001034-35).

Here, we hypothesised that targeting both NKG2A and PD-1/PD-L1 axes with blocking antibodies would boost the antitumour response following ATRi/RT. By interrogating published single-cell RNAseq datasets, we demonstrate the presence of highly activated NKG2A/PD-1 double-positive T cells in human head and neck tumours. Analyses in HPV$^-$ and HPV$^+$ preclinical models of head and neck cancer reveal that the frequencies of those T cells can be increased following ATRi/RT, making them an interesting target for immunotherapeutic modulation following combined RT and ATRi therapy. Using those animal models, we describe for the first time how the combination of ATRi, radiation and immunotherapy, based on dual anti-NKG2A and anti-PD-L1 immune checkpoint blockade (ATRi/RT/ImmuT), induces a robust antitumour response. Treatment efficiency is dependent on the recruitment of both CD8 and CD4 conventional T cells which display highly activated, proliferative and cytotoxic phenotypes in the tumour microenvironment (TME). Blocking antibody studies reveal that activation and proliferation of both CD8 and $CD4_{conv}$ T cells is dependent on the CD40/CD40L signalling pathway. To understand further the therapeutic effect of the combination, we also report that addition of immunotherapy to ATRi/RT significantly modulates the temporal dynamics of T cell activation and influences TCR repertoire richness, clonality, and antigen specificity in the TME. Together, these data present a strong case for rational clinical trial designs incorporating ATRi/RT followed by adjuvant doublet immunotherapy targeting NKG2A and PD-1/PD-L1.

Results

Highly activated NKG2A/PD-1 double positive T cells are present in the tumour microenvironment of HNSCC patients

The combination of anti-NKG2A and anti-PD-1/PD-L1 axis ICB has recently gained momentum in clinical settings, particularly in lung cancer. Reinvigoration of NKG2A/PD-1 double-positive cytotoxic lymphocyte cells in the tumour microenvironment (TME) could provide a mechanistic basis for the combination, including in HNSCC. Thus, we interrogated published databases in patients with HNSCC. First, analysis of the Cancer Genome Atlas (TCGA) revealed a significant positive correlation between expression of *KLRC1* (NKG2A) and both *PDCD1* (PD-1) and *CD274* (PD-L1) in HPV$^-$ and HPV$^+$ HNSCC tumours (Fig. 1A). To identify the type of immune cells expressing both *KLRC1* and *PDCD1*, we analysed single-cell RNA sequencing (scRNAseq) databases available in two previously published articles[19,20]. Interestingly, *KLRC1/PDCD1* double-positive immune cells were detected in both studies and those cells were predominantly present in tumours rather than blood (Fig. 1B and S1A). Further detailed analyses also showed that the majority of *KLRC1*+/*PDCD1*+ cells were in the CD8$^+$ T cell compartment (Fig. 1C, D and Fig. S1B, C). Tumour HPV status did not affect the frequencies of *KLRC1/PDCD1* double-positive CD8 and CD4 T cells (Fig. S2). Additionally, we observed that *KLRC1/PDCD1* double-positive CD8 T cells were highly activated, as shown by high expression of cytotoxic/effector/memory/proliferating lymphocyte gene signatures including *GZMA*, *GZMB*, *PRF-1*, *IFNG*, *CCL5*, *TIGIT*, *LAG3*, *ITGAE*, *CD69* and *PCNA* (Fig. 1E, F and Fig. S1D, E).

Taken together, these analyses of previously published scRNAseq datasets show the presence of highly activated NKG2A/PD-1 double-positive CD8 T cells in the TME of patients with HNSCC and point towards opportunities for their clinical exploitation.

Dual anti-NKG2A and anti-PD-L1 immune checkpoint blockade enhances ATRi/RT-mediated antitumour response in head and neck cancer preclinical models

Because of the high activation status of NKG2A/PD-1 double-positive T cells and their potential as therapeutic targets, we tested whether combination of ATRi and RT increased the number of these cells in the TME using both HPV$^-$ (MOC1) and HPV$^+$ (mEER) preclinical models[21–23].

We confirmed that combined ATRi/RT delayed tumour growth and increased survival in both models when compared to single-agent treatment (Fig. 2A and Fig. S3A). Critically, ATRi/RT led to an increase of the proportions of both NKG2A/PD-1 double-positive CD8 and CD4 conventional ($CD4_{conv}$) T cells in both MOC1 and mEER ectopic (subcutaneous) tumours (Fig. 2B and Fig. S3B, C). Importantly, the addition of ATRi to RT was critical for the infiltration of such cells into tumours (Fig. S4A). Those cells were more activated than their NKG2A/PD-1 double-negative counterparts, as shown by higher expression levels of activation/memory/proliferation markers, such as CD44, CD69, GZMB, ICOS, PRF-1, Ki67, KLRG1, NKG2D and TIM-3 (Fig. 2C). Despite a less pronounced difference in the expression of the various markers, NKG2A/PD-1 double-positive populations displayed generally a higher activation status than the PD-1 single-positive populations, (Fig. 2C). Of note, increased proportions of NKG2A/PD-1 double-positive CD8 and $CD4_{conv}$ T cells were accompanied by a greater number of cancer cells expressing both Qa-1b and PD-L1, the ligands for NKG2A and PD-1, respectively (Fig. 2D and Fig. S3D). These results strengthen the hypothesis that ATRi/RT can create a TME in which the NKG2A/Qa-1b and PD-1/PDL-1 axes might favourably be targeted concomitantly.

Next, mice bearing ectopic MOC1, MOC2 (both HPV$^-$), mEER and TC1 (both HPV$^+$) tumours received systemic anti-NKG2A and/or anti-PD-L1-blocking antibodies after ATRi/RT. Interestingly, the combination of both anti-NKG2A and PD-L1 antibodies significantly improved ATRi/RT treatment in terms of tumour growth and survival in all models (Fig. 2E, Fig. S3E and Fig. S5A, B). The addition of anti-NKG2A was necessary, as anti-PD-L1 antibody treatment alone exerted relatively modest benefits. The addition of ATRi was essential for efficacy of the full combination therapy (Fig. S4B). Importantly, the actual therapeutic benefit of having the full combination of ATRi/RT/anti-NKG2A/anti-PD-L1 was further confirmed orthotopically in both MOC1 and mEER models. When compared with the other treatment groups, mice treated with the full combination had better tumour control

https://doi.org/10.1038/s41467-024-51236-6

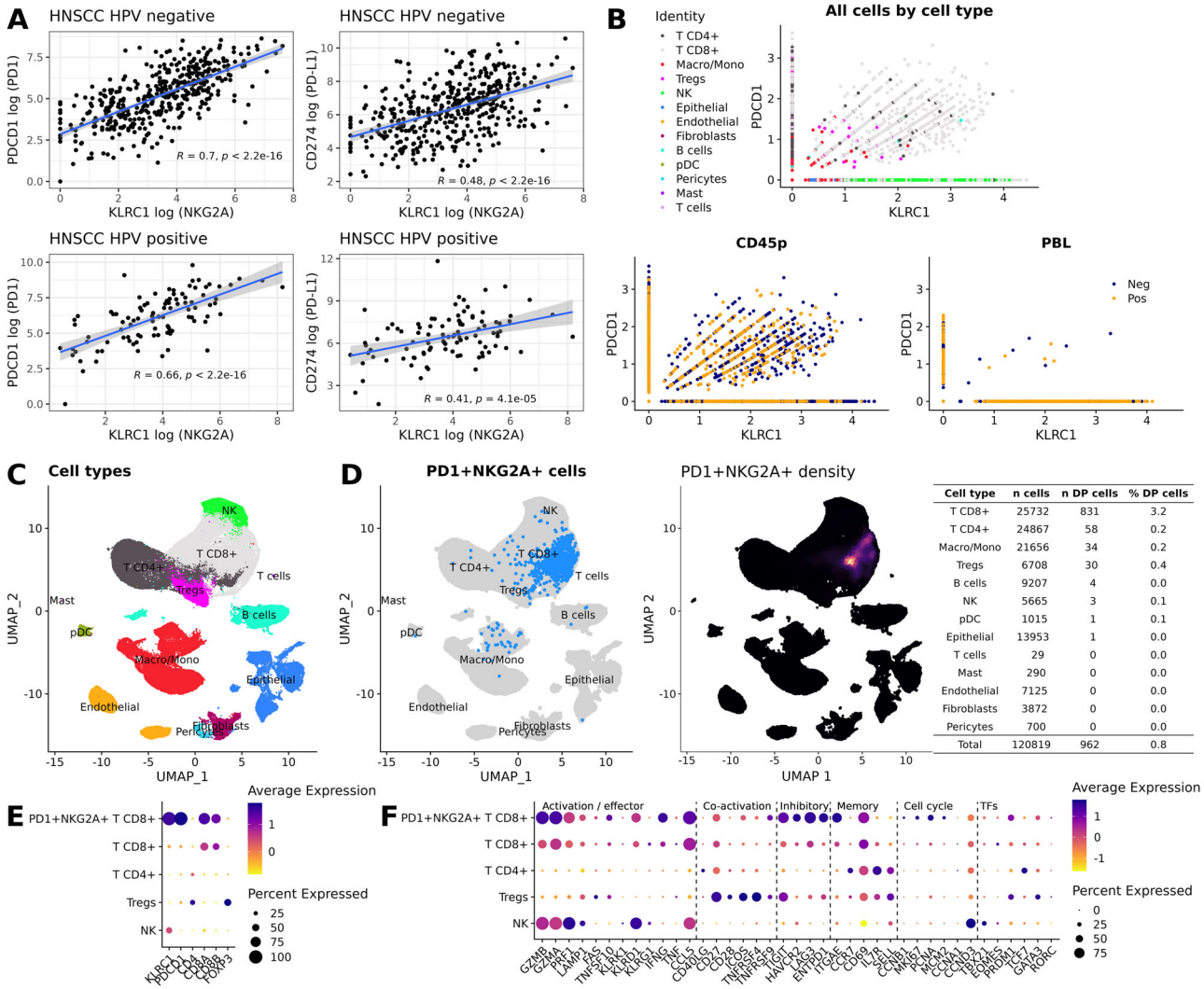

Fig. 1 | Highly activated NKG2A and PD-1 double-positive T cells are detected in patients with head and neck cancer. A TCGA database analyses of the correlation between expression of *KLRC1* and both *PDCD1* and *CD274* in both HPV$^-$ and HPV$^+$ HNSCC patients. The blue line and the shaded area indicate the linear regression fit with the 95% confidence interval; two-tailed test p-values are provided for Spearman's rank correlation coefficients. **B** Scatter plots showing expression of *KLRC1* and *PDCD1* in various cell populations (higher panel) and tumours versus blood (lower panels). **C** UMAP plot showing distribution of identified cell clusters distribution. **D** Left panel; UMAP plot depicting NKG2A/PD-1 double positive cells in the different identified cell clusters, right panel; UMAP plot depicting intensity expression of NKG2A/PD-1 double positive cells with absolute numbers for each identified cell populations (right table). Dot plots showing average and percentage expression of the *KLRC1*, *PDCD1* and pan-cell markers (**E**) and activation/effector, co-activation, inhibitory, memory, cell cycle and transcription factors (TFs) markers (**F**) in NKG2A$^+$/PD-1$^+$ CD8$^+$ T cells versus CD8$^+$T, CD4$^+$T, Tregs and NK cells. Datasets from Kurten et al.[19].

(Fig. 2F and Fig. S3F). Previously cured animals did not develop tumours on rechallenge in both models (Fig. 2G and Fig. S3G). Importantly, the full combination therapy did not trigger significant toxicity, as assessed by weight loss, throughout treatment duration in all models studied (Fig. S6).

Finally, the crucial importance of intact tumour-draining lymph nodes (TDLN) in generating and sustaining an effective anti-tumour immune response and, thereafter, clinically meaningful responses to ICB, is increasingly recognised. We, therefore, sought to validate that radiotherapy delivery in our lip orthotopic pre-clinical studies was tumour site-specific by using γ-H2AX staining as an acute radiobiological readout (Fig. S7). Unirradiated tissues showed marginal γ-H2AX staining when compared to the tumour irradiation group, where only tumours, and not TDLNs or uninvolved LNs, showed high levels of γ-H2AX staining. Irradiation of both tumours and TDLNs in separate radiation fields yielded high levels of γ-H2AX staining in both the tumour and TDLN with no signal present in the distant, unirradiated sub-iliac LN (Fig. S7).

Taken together, these data show that ATRi/RT increased the frequencies of both NKG2A$^+$/PD-1$^+$ CD8 and CD4$_{conv}$ T cells, alongside Qa-1b$^+$/PD-L1$^+$ cancer cells in the TME. Subsequent adjuvant therapy with NKG2A and PD-L1 blocking antibodies after ATRi/RT stimulated favourable effector and memory antitumour immunity in both HPV- and HPV+ head and neck cancer preclinical models.

Combination of ATRi/RT and anti-NKG2A/PD-L1 dual immune checkpoint blockade induces gene signatures characteristic of T cell activity

To study the nature of the antitumour immune response following ATRi/RT, we performed RNA sequencing (RNAseq) in MOC1, mEER and MOC2 tumours on day 11 post-radiation (8 days after the beginning of immunotherapy). Differential gene expression (DEG) analysis showed significant changes induced by ATRi/RT, which were further increased by adding immunotherapy (Fig. 3A, Fig. S8A and Fig. S9A). Volcano plots also revealed higher expression of genes typical of an immune response, such as *PRF-1*, *CD274* and

https://doi.org/10.1038/s41467-024-51236-6

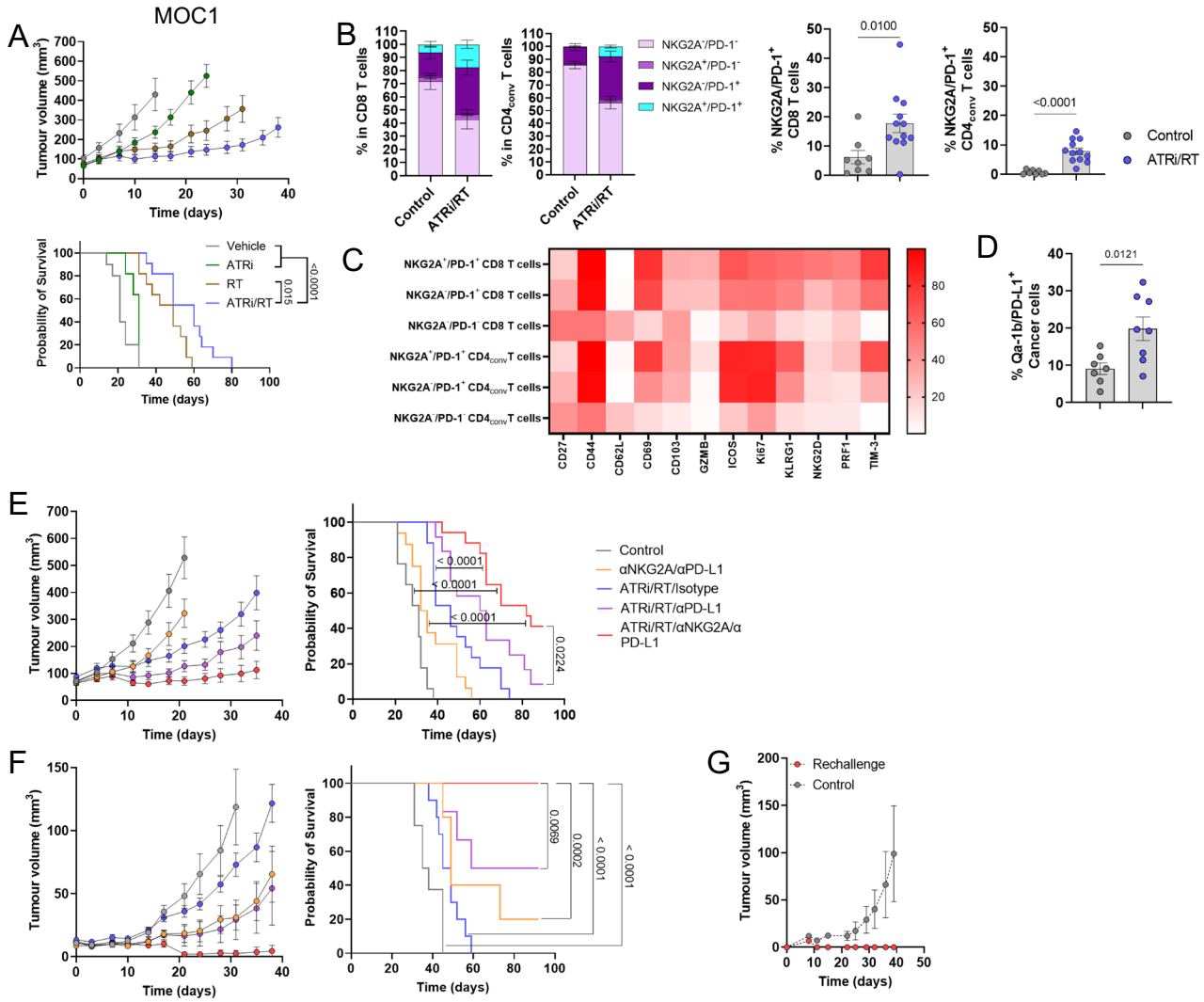

Fig. 2 | NKG2A and PD-1/PD-L1 axis immune checkpoint blockade improves the therapeutic outcome of ATRi/RT. Experiments in this figure were performed in the MOC1 model. **A** Tumour growth and survival curves across the different conditions (Control $n = 10$, ATRi $n = 11$, RT $n = 11$, ATRi/RT $n = 11$; combined from two independent experiments). **B** Bar chart; % of NKG2A and/or PD-1 positive populations in CD8 and $CD4_{conv}$ T cells, scatter plot with bar; NKG2A/PD-1 positive populations in CD8 and $CD4_{conv}$ T cells (Control $n = 8$, ATRi/RT $n = 12$; combined from two independent experiments). **C** Heatmap showing marker intensity of expression in $NKG2A^+/PD\text{-}1^+$ versus $NKG2A^-/PD\text{-}1^-$ CD8 and $CD4_{conv}$ T cells. **D** % surface expression of Qa-1b/PD-L1 double positive cancer cells in the different conditions (Control $n = 8$, ATRi/RT $n = 8$; from one experiment). Tumour growth and survival curves across the different conditions in ectopic (**E**; control $n = 17$, αNKG2A/αPD-L1 $n = 17$, ATRi/RT $n = 16$, ATRi/RT/αPD-L1 $n = 12$, ATRi/RT/αNKG2A/αPD-L1 $n = 17$; combined from three independent experiments) and orthotopic (**F**; Control $n = 8$, αNKG2A/αPD-L1 $n = 5$, ATRi/RT $n = 10$, ATRi/RT/αPD-L1 $n = 6$, ATRi/RT/αNKG2A/αPD-L1 $n = 12$; combined from two independent experiments). **G** Tumour growth in control versus rechallenged mice (Rechallenge $n = 5$, Control $n = 6$; from one experiment). Results are shown as means ± SEM and n represents number of mouse/groups. Parametric statistics were only applied to normally distributed data. Numbers on graphs represent P values and were determined by Two-tailed Unpaired t test (**A**, CD4conv T cells and **D**), Two-tailed Mann–Whitney test (**A**, CD8 T cells) and Log-Rank Mantel–Cox test (**C**, **E**, **F**).

CD8a, when mice were treated with the full combination therapy (Fig. 3B, Fig. S8B and Fig. S9B).

Immune cell population estimates from transcriptomic data, using mMCP-counter, highlighted the prominence of T cells in all models in response to treatment (Fig. 3C, Fig. S8C and Fig. S9C). However, there were some differences between models in the case of monocytes, granulocytes and fibroblasts. Analysis of single gene expression showed that, in both MOC1 and MOC2 models, ATRi/RT/anti-NKG2A/anti-PD-L1 (ATRi/RT/ImmuT) combination, when compared with the other groups, regularly induced more interferon signalling (*CD274, RSAD2, ISG15, IFIH1, DDX60* and *ZPD1*), chemoattraction (*CCL5, CCL9* and *CXCL10*), MHCI- (*H2-Aa, H2-D1, H2-M3* and *H2-T23*) and MHCII-related (*H2-AA, H2-AB1, H2-EB1, CD74* and *H2-DMB1*) gene expression (Fig. 3D and Fig. S9D). Generally, differences were less pronounced in the mEER model, with the exception of MHCII-related genes (Fig. S8D). For immune cell population gene signatures, in response to ATRi/RT/ImmuT, the lowest numerical p-values were observed for various NK cell receptors, such as *KLRD1, KLRC1* and *KLRK1* in MOC1/MOC2 tumours but only *KLRD1* and *KLRK1* in mEER tumours (Fig. 3E, Fig. S8E and Fig. S9E). It is remarkable that, in all models, we observed greater increases of genes characteristic of T cell activity, including *CD3D*, *CD3E*, *FOXP3* and *CD8A*, in response to ATRi/RT/ImmuT (Fig. 3E, Fig. S8E and Fig. S9E). Finally, we also detected in the same treatment group high expression of genes for immune cell activation markers, including *GZMB, PRF1, PDCD1, HAVCR2, ICOS, TNFRSF4, CD40, CD27* and *CD28*, in all tumours (Fig. 3F, Fig. S8F and Fig. S9F).

Together, RNAseq analysis suggests that ATRi/RT and anti-NKG2A/PD-L1 dual immune checkpoint blockade triggers a robust immune response in the TME, which is likely to be mediated by the

https://doi.org/10.1038/s41467-024-51236-6

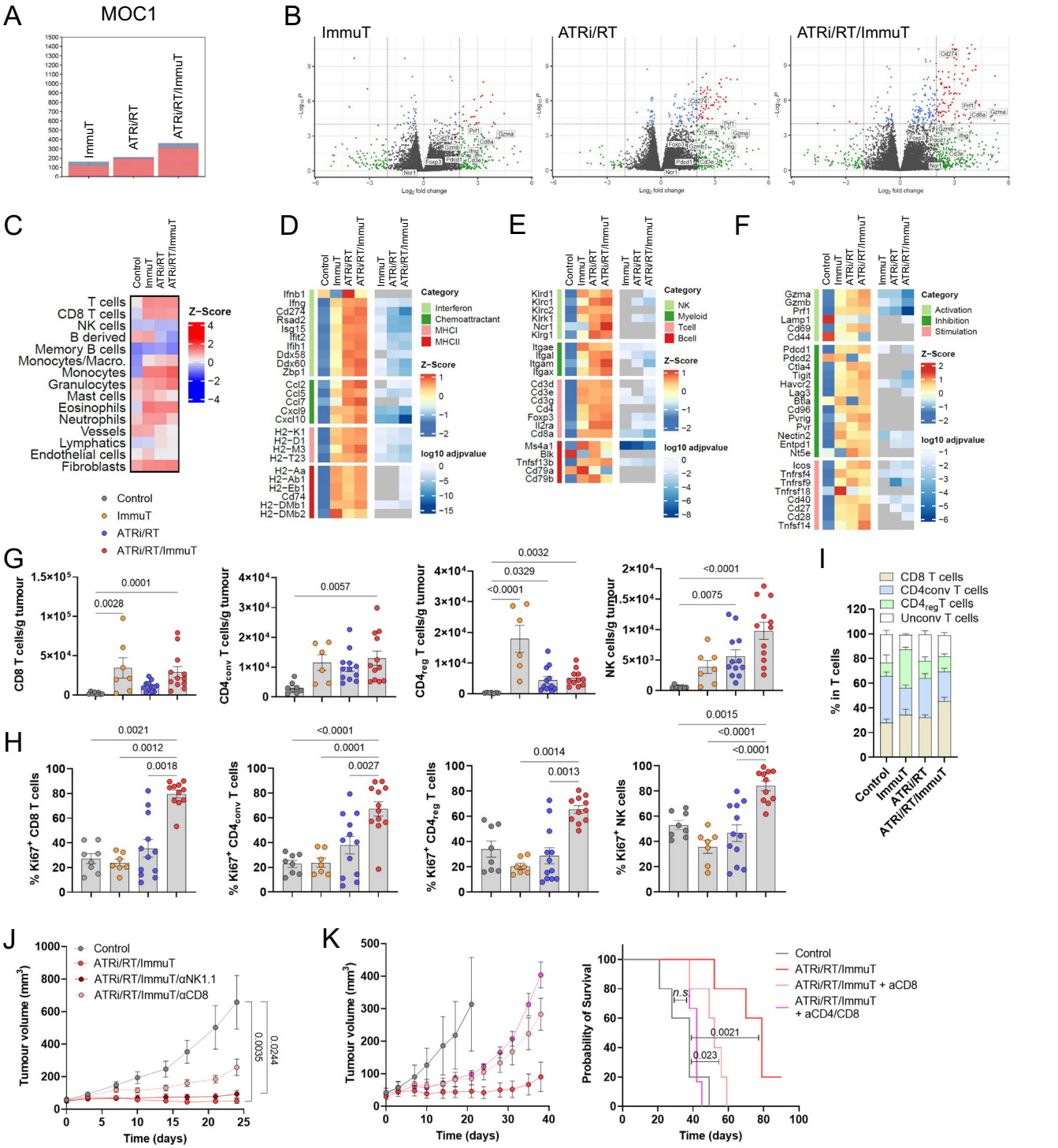

activity of T cells in both HPV⁻ and HPV⁺ head and neck cancer models.

The efficacy of the combination of ATRi/RT and anti-NKG2A/PD-L1 immunotherapy is dependent on the activity of both CD8 and CD4 T cells

To confirm the RNAseq results, we performed flow cytometry analyses in both MOC1 and mEER tumours. The lymphocyte data revealed that full combination therapy with ATRi/RT/ImmuT significantly induced greater infiltration of CD8, $CD4_{conv}$ and CD4 regulatory (reg) T cells, as well as NK cells, into the TME in both models in comparison with the other treatment groups (Fig. 3G and Fig. S8G). Of note, ATRi/RT or ImmuT on their own did significantly boost the infiltration of some lymphocyte subtypes, such as CD8 and $CD4_{conv}$ T cells, in some instances. Importantly, however, only the full ATRi/RT/ImmuT combination led to a significant improvement of lymphocyte activation as demonstrated by increased intracellular expression of the pan-activation/proliferation marker Ki67 (Fig. 3H and Fig. S8H). In addition, in respect of T cell compartment, ATRi/RT/ImmuT caused increased frequencies of CD8 T cells (Fig. 3I and Fig. S8I). Finally, to prove specific reactivity of T cells towards tumour antigens, we restimulated splenocytes from mEER tumour-bearing mice treated with the different therapies with a long overlapping HPV16 E7 peptide pool. Only full combination therapy significantly increased the proportions of both

Fig. 3 | ATRi/RT and anti-NKG2A/PD-L1 immunotherapy trigger a potent T-cell antitumour immune response. Experiments presented in this figure were performed in the MOC1 model. RNAseq experiments were performed with $n = 4$ for each group (**A**) Number of differentially expressed genes (DEGs) across the different conditions calculated by DESeq2 using Wald test. **B** Volcano plots showing expression of the different genes in the various conditions (genes characteristic of an immune response are named). **C** Immune cell population estimates. Immune cell scoring was performed on normalised RNAseq counts using the mMCP-counter package. Heatmaps corresponding to interferon and cytokine signalling, chemoattractant, MHCI and MHCII (**D**); immune cell populations (**E**); and immune cell activation status (**F**). Data shown are z-scores of log2 transformed normalised counts for the treatment conditions shown. This plotted alongside log10 adjusted *p*-value for each gene calculated from DEG analysis using Wald test. Non-significant adjusted *p*-values > 0.05 are indicated as grey. **G** Absolute number/gram of tumour of the indicated lymphocytes in the various conditions (Control $n = 8$, ImmuT $n = 7$, ATRi/RT $n = 12$, ATRi/RT/ImmuT $n = 12$; combined from two independent experiments). **H** % Ki67-positive cells in the indicated lymphocytes in the different conditions (Control $n = 8$, ImmuT $n = 7$, ATRi/RT $n = 12$, ATRi/RT/ImmuT $n = 12$; combined from two independent experiments). **I** % indicated lymphocytes in the total T cell population across all treatment conditions (Control $n = 8$, ImmuT $n = 7$, ATRi/RT $n = 12$, ATRi/RT/ImmuT $n = 12$; combined from two independent experiments). **J** Tumour growth curves across all conditions (Control $n = 5$, ATRi/RT/ImmuT $n = 6$, ATRi/RT/ImmuT/aNK1.1 $n = 5$, ATRi/RT/ImmuT/aCD8 $n = 6$; from one experiment). **K** Tumour growth and survival curves across the different conditions (Control $n = 5$, ATRi/RT/ImmuT $n = 5$, ATRi/RT/ImmuT/aCD8 $n = 5$, ATRi/RT/ImmuT/aCD4/CD8 $n = 6$; from one experiment). Results are shown as means ± SEM and *n* represents number of mouse/groups. Parametric statistics were only applied to normally distributed data. Numbers on graphs represent *P* values and were determined by Kruskal–Wallis test with Dunn's multiple comparison test (**G**; CD8 T cells, $CD4_{reg}$ T cells and NK cells; H; CD8 T cells, $CD4_{reg}$ T cells and NK cells), ordinary one-way ANOVA with Tukey's multiple comparison test (**G**; $CD4_{conv}$ T cells and **H**; $CD4_{conv}$ T cells), Kruskal–Wallis test with Dunn's multiple comparison test from area under curve (**J**) and Log-Rank Mantel–Cox test (**K**). Significant outliers were removed using Grubb's test.

CD8 and $CD4_{conv}$ T cells with proliferative and cytotoxic capacities (Fig. S8J).

In light of those data, we defined the subtypes of lymphocytes mediating treatment efficacy using specific depleting antibodies. In mice treated with ATRi/RT/ImmuT, the acceleration of tumour growth and shortened lifespan in the absence of CD8 T cells demonstrated the crucial role of those cells in mediating therapy in the MOC1 and MOC2 models (Fig. 3J and Fig. S9G). The effect of CD8 T cells was even more marked in the mEER model (Fig. S8K). In contrast to CD8 T cells, however, depletion of NK cells did not have a significant effect on the efficacy of the full combination treatment, except in the MOC2 model (Fig. 3J, Fig. S8K and Fig. S9G). Strikingly, the depletion of both CD8 and CD4 T cells in MOC1-bearing mice completely abrogated the effect of the full combination therapy in terms of mouse survival (Fig. 3K). Delayed separation between the tumour growth curves of CD8 and CD8/CD4 T cell-depleted mice suggests a delayed role for CD4 T cells.

Taken together, these data suggest that the efficacy of ATRi/RT/ImmuT combination therapy is dependent on the infiltration of both activated CD8 and CD4 T cells in the TME.

Combination of ATRi/RT and anti-NKG2A/-PD-L1 immunotherapy promotes the infiltration of CD8 and $CD4_{conv}$ T cell subpopulations with a PD-1^{high} cytotoxic/proliferative/effector memory phenotype

Next, we sought insight into the specific phenotypes of therapy-related tumour-infiltrating CD8 and CD4 T cells. Thus, we performed extensive immune profiling in the MOC1 model, using a combination of TriMap and FlowSOM algorithms to identify the various clusters of CD8 and CD4 T cell populations in control and treatment groups.

We observed a disappearance of naïve/inactivated CD8 and CD4 T cell populations (pop 4 and 0, respectively) from MOC1 tumours. These populations were diminished in the ATRi/RT cohort and completely absent in response to the full combination therapy (Fig. 4A, B). In parallel, a shift towards populations with an activated/proliferative phenotype for CD8 T cells was identified in response to ATRi/RT (pop 6 and 7), but this effect was accentuated after the addition of immunotherapy (pop 2 and 3) (Fig. 4A). The same pattern was detected for $CD4_{conv}$ T cells, with populations displaying more pronounced activated/proliferative phenotypes (pop 3, 4, 6 and 9) in the full combination therapy when compared with ATRi/RT alone. By contrast, adding immunotherapy to ATRi/RT did not significantly modulate the various populations of $CD4_{reg}$ T cells when compared with ATRi/RT alone (Fig. 4B).

The key findings from TriMap/FlowSOM analyses were further investigated to evaluate their significance. Since increased proliferation was an important feature of T cell subpopulations infiltrating MOC1 tumours after full combination therapy, we tracked cell cycle distribution in CD8 and $CD4_{conv}$ T cells. ImmuT added to ATRi/RT caused a noticeable shift of both CD8 and $CD4_{conv}$ T cells towards G2/M phase, which suggests the presence of actively dividing cells (Fig. 4C). At the same time, we observed that ATRi/RT/ImmuT was instrumental in increasing the frequencies of PD-1^+ (Fig. 4D), $ICOS^+$ (Fig. 4E) and effector memory (EM) (Fig. 4F) CD8 and $CD4_{conv}$ T cells. In line with the TriMap/FlowSOM analysis, MOC1 tumours were more infiltrated with Ki67/$PRF1^+$ CD8 and $CD4_{conv}$ T_{EM} cells in response to the full combination (Fig. 4G). We also detected elevated frequencies of $NKG2D^+$ and T-BET^+ CD8 and $CD4_{conv}$ T cells in the same treatment group when compared with ATRi/RT alone (Fig. 4H, I).

To evaluate the specific effect of including anti-NKG2A antibody in full combination therapy at the cellular level, we performed the same set of experiments, comparing the key subpopulations of both CD8 and $CD4_{conv}$ T cells previously described between ATRi/RT, ATRi/RT/anti-PD-L1 and ATRi/RT/anti-NKG2A/PD-L1 treatment groups. Interestingly, blocking NKG2A was critical in shifting the cell cycle in CD8 T cells from G0/G1 to G2/M phases, and the same effect was seen in $CD4_{conv}$ T cells (Fig. S10A). These data were further reinforced by the significant increase of $Ki67^+$ cells in the treatment cohort that included anti-NKG2A (Fig. S10B). Adding anti-NKG2A also enhanced the frequencies of both PD-1^+ CD8 and $CD4_{conv}$ T cells and $ICOS^+$ $CD4_{conv}$ T cells (Fig. S10C, D). Anti-NKG2A antibody significantly promoted the effector memory phenotype, which correlated with increased proportions of Ki67/$PRF1^+$ CD8 and $CD4_{conv}$ T_{EM} cells (Fig. S10E, F). Finally, the inclusion of anti-NKG2A in combination therapy crucially elevated the frequencies of NKG2D- and T-BET-positive CD8 and $CD4_{conv}$ T cells (Fig. S10G, H).

Taken together, these data indicate that ATRi/RT/anti-NKG2A/PD-L1 combination therapy leads to the infiltration of PD-1^{high}/cytotoxic/proliferative/effector memory CD8 and $CD4_{conv}$ T cells in the TME. In parallel and importantly, the nature of $CD4_{reg}$ T cell populations following ATRi/RT is not affected by the addition of anti-NKG2A/PD-L1 immune checkpoint blockade.

CD40 signalling mediates antitumour immunity in response to ATRi/RT/anti-NKG2A/PD-L1 combination therapy

As described above, prominent subpopulations of both CD8 and $CD4_{conv}$ T cells in the TME following ATRi/RT/ImmuT were characterised by high surface expression of PD-1. We detected in similar experiments enhanced expression of CD40L on those PD-1^+ T cells, i.e., the most activated cells (Fig. 5A). In parallel, the same treatment conditions led to an increase of CD40^{high} cDC1, cDC2 and pDCs, as well as $CD40^+$ monocytes, macrophages and neutrophils (Fig. S11A, B). These findings prompted evaluation of whether CD40/CD40L signalling was a potential costimulatory pathway responsible for the therapeutic effect seen.

https://doi.org/10.1038/s41467-024-51236-6

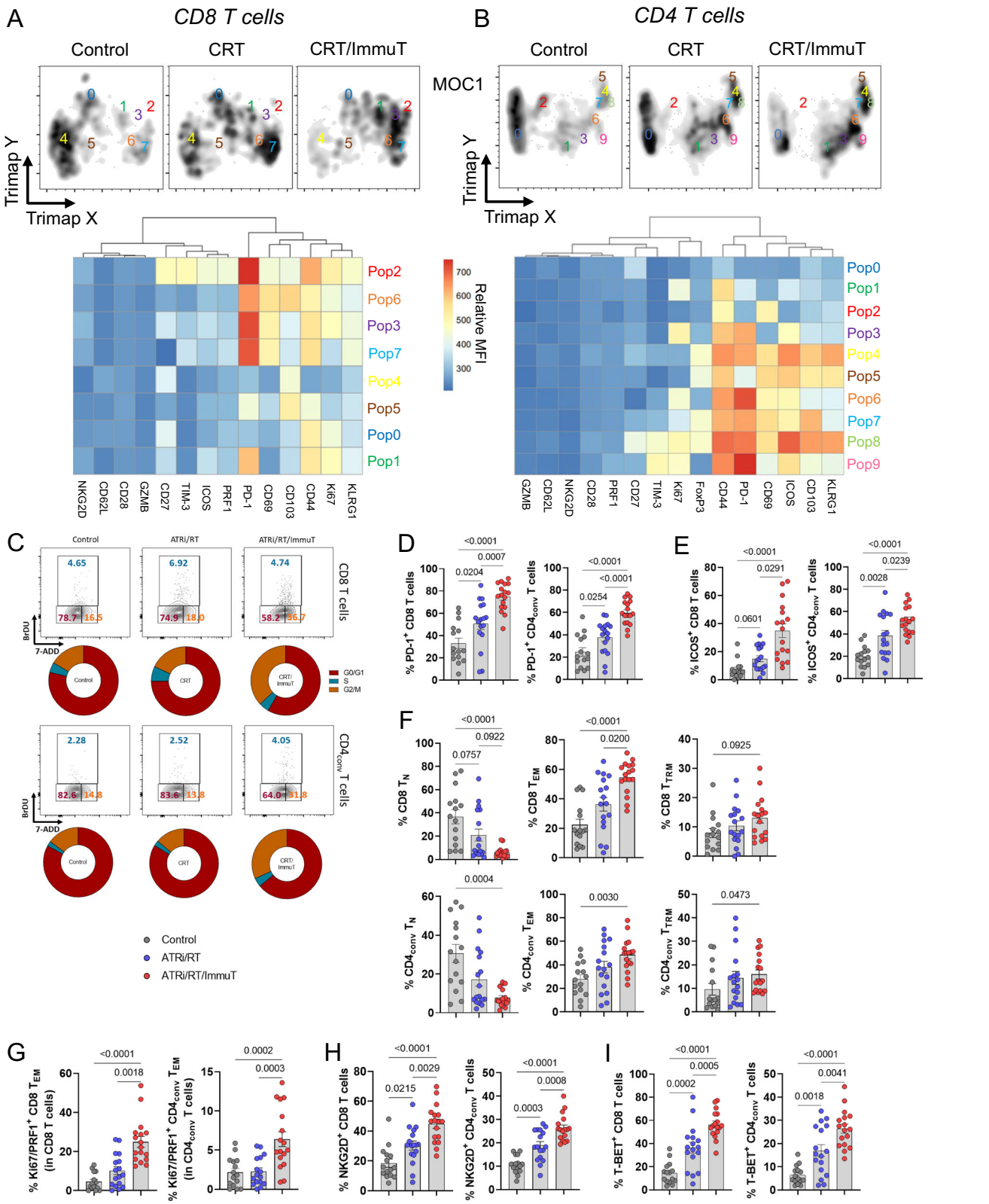

Indeed, we found that stimulation of CD40 following ATRi/RT significantly reduced tumour burden (Fig. S10C), whereas interfering with CD40/CD40L signalling abrogated the additive therapeutic effect of immune checkpoint blockade (Fig. 5B, C). Furthermore, blocking this costimulatory pathway decreased infiltration of both CD8 and $CD4_{conv}$ T cells (Fig. 5D) and remaining tumour-infiltrating CD8 and $CD4_{conv}$ T cells lost PD-1 expression, effector memory status, proliferative and cytotoxic capacities (Fig. 5E, F). Finally, to highlight the translational potential of this findings, analysis of the TCGA database revealed that both *CD40* and *CD40LG* expression significantly correlated with *KLRC1* and *PDCD1* expression in HNSCC patients, regardless of their HPV status (Fig. 5G).

Taken together, these results demonstrate that CD40/CD40L signalling plays a key role in mediating the full efficacy of ATRi/RT/

Fig. 4 | ATRi/RT and anti-NKG2A/PD-L1 immunotherapy induce the proliferation of PD-1$^+$ effector memory cytotoxic CD8 and CD4 T-cells in the tumour microenvironment. Experiments presented in this figure were performed in the MOC1 model. **A**, **B** Higher panels; intensity of the different subpopulation clusters of CD8 (**A**) and CD4 (**B**) T cells identified using TriMap and FlowSOM algorithms, lower panels; heatmap showing the expression of the indicated markers in the different populations identified by FlowSOM algorithm across all treatment conditions (concatenated from Control $n = 7$, ATRi/RT $n = 8$, ATRi/RT/ImmuT $n = 8$; from one experiment). **C** Dot plot and donut chart representing % of CD8 and $CD4_{conv}$ T cells in the different cell cycle phases across all conditions (concatenated from Control $n = 5$, ATRi/RT $n = 6$, ATRi/RT/ImmuT $n = 6$; from one experiment). Across all conditions the following graphs show % (**D**) PD-1$^+$, (**E**) ICOS$^+$, (**F**) naïve (N; CD62L$^+$ CD44$^-$), effector (EM; CD62L$^-$ CD44$^+$ CD103$^-$) and tissue-resident (TRM; CD62L$^-$ CD44$^+$ CD103$^+$) memory, (**G**) Ki67/PRF$^+$ EM, (**H**) NKG2D$^+$ and (**I**) T-BET$^+$ CD8 and $CD4_{conv}$ T cells (Control $n = 15$, ATRi/RT $n = 17$, ATRi/RT $n = 17$; combined from two independent experiments). Results are shown as means ± SEM and n represents number of mouse/groups. Parametric statistics were only applied to normally distributed data. Numbers on graphs represent P values and were determined by Kruskal-Wallis test with Dunn's multiple comparison test (**E**; CD8 T cells; **F**; CD8 T_N, CD4conv T_N, CD8 T_{EM}, $CD4_{conv}$ T_{TRM}; **G**; CD8 T cells) or ordinary one-way ANOVA with Tukey's multiple comparison test (**E**; $CD4_{conv}$ T cells, **F**; $CD4_{conv}$ T_{EM}, CD8 T_{TRM}; **G**; $CD4_{conv}$ T cells; **H**, **I**).

ImmuT by promoting the infiltration and activation of highly activated, proliferating CD8 and $CD4_{conv}$ T cells.

Combination of ATRi/RT and anti-NKG2A/-PD-L1 immunotherapy significantly affects the dynamics of TCR activity

To study the temporal progression and dynamics of T cell activity in response to combination therapies, we used the recently developed "Timer and Cell Kinetics and Activity" (Tocky) system[24,25]. Tocky is a reporter system based on a fluorescent 'Timer' protein, which spontaneously changes its emission from blue to red within 4 h (Fig. 6A). The red-form protein is stable, so its maturation allows flow cytometric-based monitoring of rapid temporal changes in expression. By using transgenic mice in which the expression of fluorescent Timer protein is synchronised with the Nr4a3 gene (Nr4a3-Tocky), we can study the induction of TCR activation. Resting T cells do not express the Timer protein (negative signal) but, once T cells recognise cognate antigen and receive TCR signals, Timer transcription is initiated and they become blue$^+$ red$^-$ (new signal). T cells with persistent TCR signalling sustain Timer transcription over time and accumulate both blue$^+$ and red$^+$ proteins (persistent signal). When T cells disengage from their antigens, Timer transcription is arrested, and the unstable blue$^-$ protein is lost, resulting in T cells becoming blue$^-$ red$^+$ (arrested signal) (Fig. 6A).

NKG2A/PD-1 double-positive CD8 and $CD4_{conv}$ T cells were characterised by increased frequencies of persistent TCR activation when compared to other subpopulations (Fig. 6B). Additionally, CD40L$^+$ CD8 and $CD4_{conv}$ T cells were more persistent than the CD40L$^-$ population (Fig. S12A). The action of combined ATRi/RT/ImmuT significantly reduced the proportions of Timer-negative CD8 and $CD4_{conv}$ T cells, which demonstrated enhanced TCR engagement (Fig. 6C). No variations were observed in terms of new TCR signalling in CD8 T cells across all treatment groups (Fig. 6C). In contrast, we observed significantly higher proportions of new TCR signals in $CD4_{conv}$ T cells with the addition of ImmuT to ATRi/RT (Fig. 6C). Whilst there was a trend towards a decrease in the same new Timer population in $CD4_{reg}$ T cells, we detected a significant increase in the frequencies of CD8 T cells with persistent TCR signal in response to ATRi/RT/ImmuT (Fig. 6C). Trends for increased proportions of persistent $CD4_{conv}$ T cells were found in both ATRi/RT and ATRi/RT/ImmuT treatment groups (Fig. 6C). Persistence of TCR activation in both CD8 and $CD4_{conv}$ T cells was significantly dependent on CD40/CD40L signalling (Fig. S12B, C). There was no impact in the frequencies of arrested TCR signalling in all T cells under any treatment condition. Interestingly, populations of CD8 and $CD4_{conv}$ T cells with high Timer intensity were enriched for PD-1 and CD44 but devoid of CD62L, which highlighted their PD-1$^+$ effector memory status (Fig. 6D), as shown by Uniform Manifold Approximation and Projection (UMAP) analysis of Timer Angle and Intensity with markers[26].

Taken together, these data show unique dynamics of TCR activity from the various populations of T cells in the TME after treatment. Only with the full ATRi/RT/ImmuT combination did CD8 T cells display more persistent TCR activation, while $CD4_{conv}$ T cells exhibited more recent TCR engagement. Importantly, however, the dynamics of TCR activity in $CD4_{reg}$ T cells was not significantly impacted by the different therapeutic regimens, suggesting a more prominent T cell signalling function for $CD4_{conv}$ T cells in cooperation with CD8 T cells.

Combination of ATRi/RT and anti-NKG2A/PD-L1 immune checkpoint blockade induces variations of TCR repertoires in tumours

To follow up on Tocky analyses and to explore further the amplitude of T cell antitumour response, we subsequently evaluated TCR repertoires in response to different therapy groups. RNA-based targeted sequencing of the CDR3B chain of the TCR was performed from fresh-frozen tumours from mice under three different conditions (control, ATRi/RT and ATRi/RT/ImmuT).

Only the ATRi/RT/ImmuT combination was associated with a significantly higher number of absolute unique productive clonotypes compared to the control, which suggests an increase in TCR repertoire richness (Fig. 7A). Next, Gini Simpson coefficient was used to quantify clonality across the different conditions. We found that only the full combination showed a significantly higher TCR repertoire clonality compared to the control, suggesting intra-tumoral T-cell expansion (Fig. 7B). However, no differences were found between the ATRi/RT and the addition of ImmuT. This was also confirmed when exploring the proportion of the repertoire occupied by the first quintile (Q1), which was found to be higher compared to the control in both ATRi/RT and ATRi/RT/ImmuT arms (Fig. 7C, D). The V- and J-usage did not significantly change across the different conditions, although a trend towards an increase in the even distribution of the V- and J- gene segment pairing was observed when immunotherapy was added to ATRi/RT (Fig. 7E). When clustering the expanded TCRs by CDR3B triplet amino acid similarity (Fig. 7F), we found that only the full combination displayed a significant increase in the normalised cluster count compared to the control (Fig. 7G). Furthermore, these clusters of closely similar TCR clonotypes were not only more abundant, but also bigger in size in the ImmuT-containing combination, as shown when comparing the number of dominant clusters defined as those formed by ≥3 expanded clonotypes (Fig. 7G). This observation strongly supports the notion that the addition of ImmuT to ATRi/RT leads to preferential expansion of large clusters of antigen-sharing T-cell clonotypes, which may reflect enhanced stimulation by increased antigen cross-presentation and T-cell priming, and/or the ability of this combination to promote primed T-cell activation and expansion. Furthermore, the effect of adding anti-CD40L to the triple combination was interrogated. Blocking treatment with anti-CD40L significantly affected the TCR repertoire by abolishing the effect of ATRi/RT/ImmuT in TCR richness (Fig. S13A), clonality (Fig. S13B, C) and antigen-sharing clustering (Fig. S13D, E).

Together, this strongly suggests that the intra-tumoral adaptive immune effects of ATRi/RT and ATRi/RT/ImmuT require engagement of CD40-CD40L signalling, contributing to T cell expansion and TCR repertoire remodelling.

https://doi.org/10.1038/s41467-024-51236-6

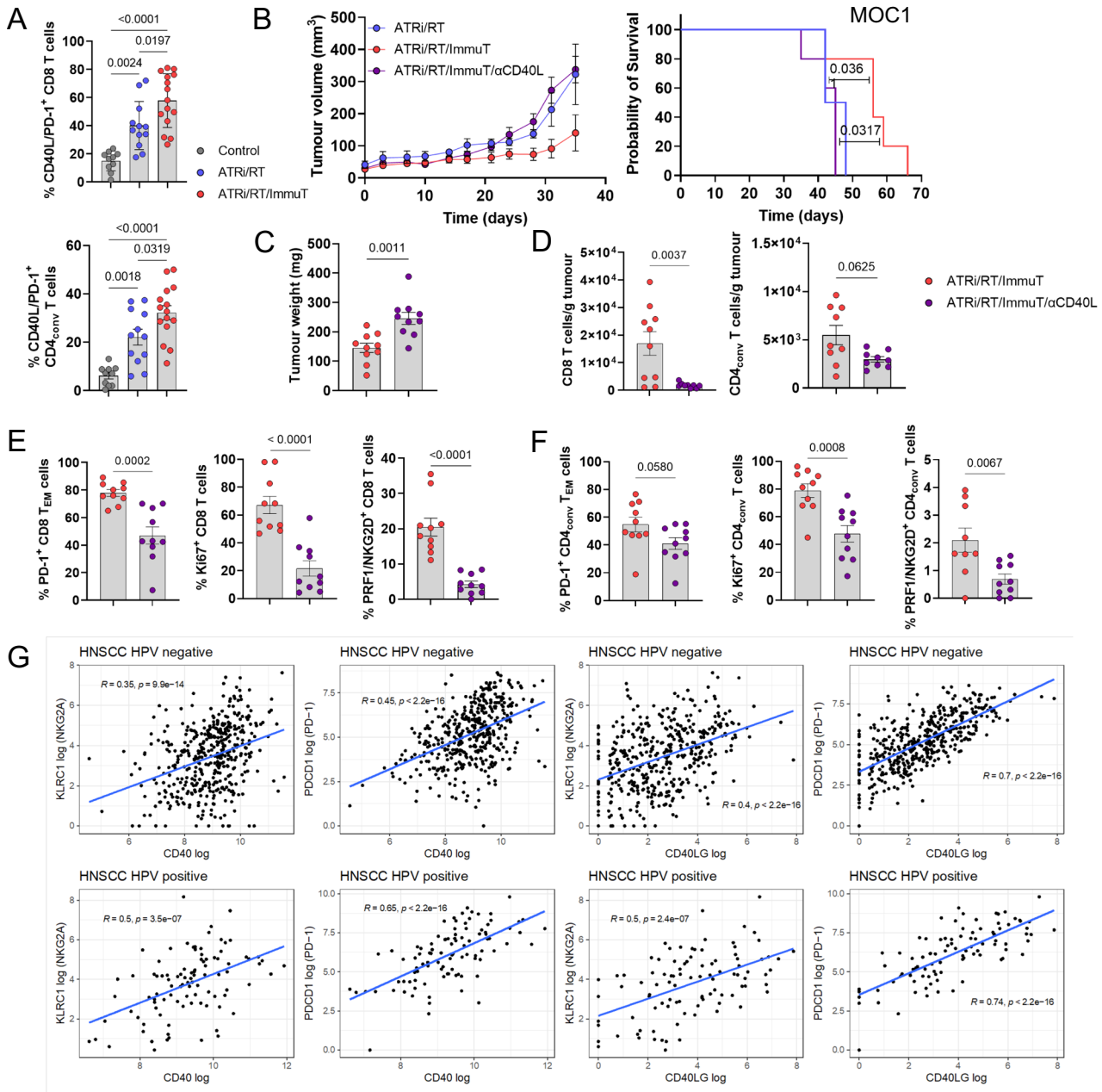

Fig. 5 | CD40 signalling mediates the efficacy of ATRi/RT and immunotherapy combination. Experiments presented in this figure were performed in the MOC1 model. **A** % of PD-1/CD40L double positive CD8 and $CD4_{conv}$ T cells across indicated treatment conditions (Control $n = 10$, ATRi/RT $n = 12$, ATRi/RT/ImmuT $n = 15$; combined from three independent experiments). **B** Tumour growth and survival curves across the different conditions ($n = 5$ for each group; from one experiment). **C** Tumour weight collected from mice in the indicated conditions ($n = 10$ for each group; from one experiment). **D** Absolute number/gram of tumour tissue of CD8 and $CD4_{conv}$ T cells in the various conditions ($n = 10$ for each group; from one experiment). % $PD\text{-}1^+$, $Ki67^+$ and $PRF/NKG2D^+$ CD8 (**E**) and $CD4_{conv}$ (**F**) T cells in treatment conditions ($n = 10$ for each group; from one experiment). **G** TCGA database analyses of the correlation between expression of *KLRC1* and *PDCD1* with *CD40* and *CD40LG* in both HPV^- and HPV^+ HNSCC patients. The blue line and the shaded area indicate the linear regression fit with the 95% confidence interval; two-tailed test p-values are provided for Spearman's rank correlation coefficients. Results are shown as means ± SEM and *n* represents number of mouse/groups. Parametric statistics were only applied to normally distributed data. Numbers on graphs represent *P* values and for in vivo experiments were determined by ordinary one-way ANOVA with Tukey's multiple comparison test (**A**); Log-Rank Mantel–Cox test (**B**) and Two-tailed Unpaired *t* test (**C**–**F**). Significant outliers were removed using Grubb's test.

Discussion

The development of novel therapeutic interventions to eradicate cancer in the future will certainly require, among other approaches, a focus on the most efficient ways to combine targeted therapy, radiation and ICB. Previous clinical trials on the combination of chemoradiotherapy and anti-PD-1/PD-L1 have shown successful results, particularly in the context of lung cancer[27–29]. However, the outcomes of equivalent strategies in head and neck cancer patients have been disappointing to date[4,5,30] (NCT03040999), probably because they have employed the rather blunt methodological approach of adding anti-PD1/-PD-L1 therapy to standard-of-care (chemo)radiotherapy without any consideration of baseline or on-treatment TME biology. It is highly likely that addition of other immune modulating therapies will be necessary to fine-tune the TME against malignant cells during or following chemoradiotherapy. One such candidate is the anti-NKG2A antibody, monalizumab, which is

https://doi.org/10.1038/s41467-024-51236-6

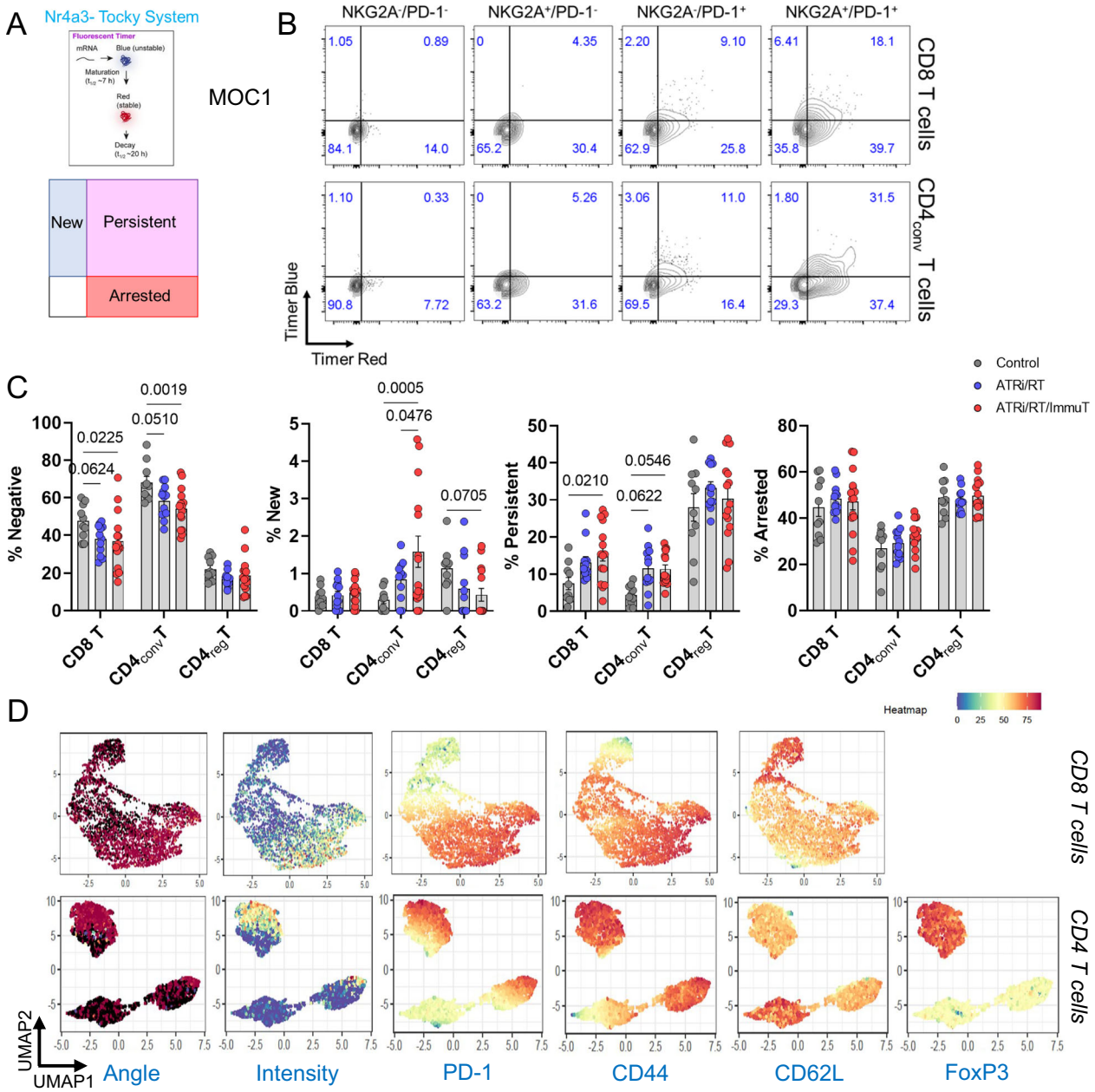

Fig. 6 | RT, DDRi and anti-NKG2A/PD-L1 immunotherapy modulate the dynamics of TCR activity in both CD8 and CD4 T cells. Experiments presented in this figure were performed in the MOC1 model. **A** Higher panel; schematic explaining production and decay of the Timer protein; lower panel: gating strategy for the detection of the different Timer populations, negative, new, persistent and arrested. **B** Dot plots showing the % of the different Timer population in NKG2A$^-$/PD-1$^-$, NKG2A$^+$/PD-1$^-$, NKG2A$^-$/PD-1$^+$ and NKG2A$^+$/PD-1$^+$ CD8 and CD4$_{conv}$ T cells (concatenated $n = 6$; from one experiment). **C** % of the indicated Timer population in CD8, CD4$_{conv}$ and CD4$_{reg}$ T cells across all conditions (Control $n = 10$, ATRi/RT $n = 12$, ATRi/RT/ImmuT $n = 15$; combined from three independent experiments). **D** UMAP plot showing Tocky angle and expression intensity as well as indicated markers expression intensity (concatenated from $n = 14$, independent of condition from one experiment). Results are shown as means ± SEM and n represents number of mouse/groups. Parametric statistics were only applied to normally distributed data. Numbers on graphs represent P values and were determined by two-way ANOVA with Tukey's multiple comparison test (**C**). Significant outliers were removed using Grubb's test.

being investigated in clinical settings[10,12]. In the present study, we describe the efficacy of a combination of ATR inhibitor, radiation and anti-NKG2A/anti-PD-L1 immune checkpoint blockade in mounting a protective antitumour immune response in both HPV$^-$ and HPV$^+$ preclinical models of head and neck cancer. Enhanced antitumour functions of NKG2A$^+$ CD8 T cells have been described in previous studies. NKG2A was reported to be a late immune checkpoint and NKG2A expression in CD8 T cells was associated with repeated stimulation and cell division[31,32]. NKG2A-positive clusters of CD8 T cells in head and neck cancer patients were enriched for other immune checkpoints, including PD-1, TIM-3 and CD39[32]. Furthermore, NKG2A$^+$ CD8 T cells were characterised by a proliferative, cytotoxic and tissue-resident memory phenotype with TCR-independent functions in bladder cancer[31]. Herein, we extended those findings by showing the presence of highly activated NKG2A/PD-1 double-positive CD8 T cells in human head and neck cancer tumours. Very low numbers of double-positive CD4 T cells were detected. Interestingly, our preclinical murine results were concordant with human scRNAseq with very low NKG2A$^+$/PD-1$^+$ CD4 T cell numbers in the TME of both non-treated HPV$^-$ and HPV$^+$ tumours. Mouse studies also

https://doi.org/10.1038/s41467-024-51236-6

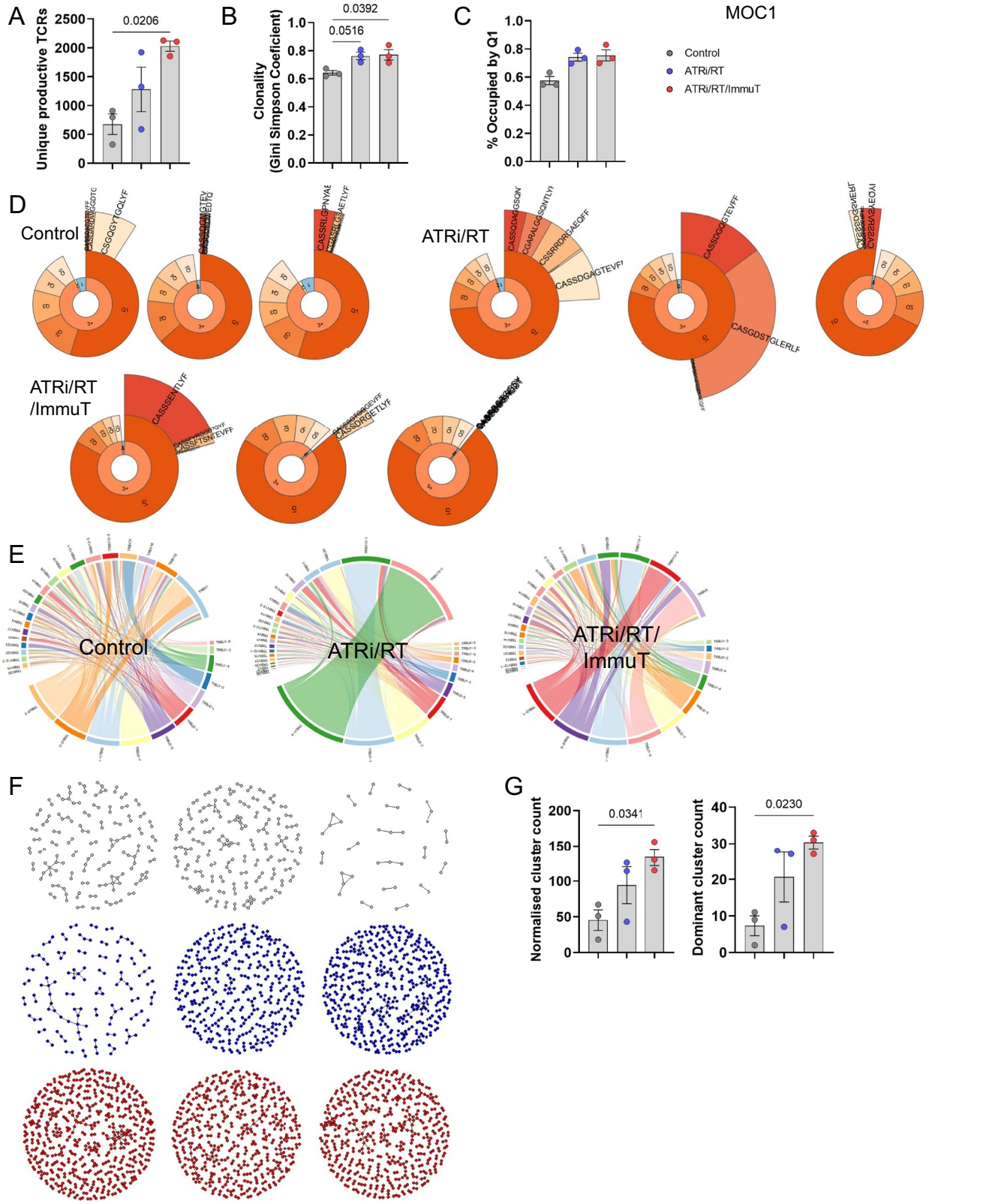

allowed us to determine that ATRi/RT led to an increase in the proportion of both NKG2A^{+}/PD-1^{+} CD8 and CD4 T cells in the TME. These findings reinforced the hypothesis that targeting NKG2A/PD-1 double-positive T cells after ATRi/RT could represent a promising therapeutic strategy. Moreover, the development of bispecific blocking antibodies targeting NKG2A and PD-1/PD-L1 axes is likely to facilitate the design of future clinical trials.

In the data reported here, not only have we demonstrated the benefit of ATRi/RT/anti-NKG2A/-PD-L1 on tumour growth and survival in both ectopic and orthotopic models, but we have also elaborated, in detail, the ability of this combination to reconfigure the biology of both CD8 and CD4 T cells in the TME. Dual anti-NKG2A/-PD-L1 immunotherapy, added as an adjuvant to ATRi/RT, drives significant infiltration of PD-1^{high}/proliferative/effector memory cytotoxic CD8 and

Fig. 7 | Variations in tumour TCR repertoire following ATR/RT and anti-NKG2A/PD-L1 immunotherapy. One single experiment was performed with $n = 3$ for each group in the MOC1 model. **A** Absolute number of unique productive clonotypes across the different conditions. **B** Clonality (Gini Simpson coefficient) across different conditions. **C** Comparison of the proportion (in percentage) of the TCR repertoire occupied by the first quantile of clonotypes. **D** Clonality plots for each condition. The plots present 3 layers to visualise the TCR repertoire clonality: the first layer includes the frequency of singleton ("1", met once), doubleton ("2", met twice) and high-order ("3+", met three or more times) clonotypes; the second layer ("quintile"), displays the abundance of top 20% ("Q1"), next 20% ("Q2"), … (up to "Q5") clonotypes for clonotypes from "3+" set; and the last layer ("top") displays the individual abundances of top 5 clonotypes. **E** Representative of V–J junctions by circus plot for each condition. Arcs correspond to different *V* and *J* segments, scaled to their frequency in samples and ribbons represent V–J pairings and their size is scaled to their pairing frequency. **F** Network diagrams of CDR3B amino acid triplet clusters for each condition. Clusters containing expanded CDR3s are shown. **G** Comparison of normalised cluster count and dominant cluster count for each condition. Results are shown as means ± SEM and *n* represents number of mouse/groups. Parametric statistics were only applied to normally distributed data. Numbers on graphs represent *P* values and were determined by ordinary one-way ANOVA with Tukey's multiple comparison test (**A**–**C**, **G**).

$CD4_{conv}$ T cells in tumours. We found that addition of anti-NKG2A antibody to the combination was essential to shifting the cell cycle towards the G2/M phase in T cells, which was in line with previous data showing repeated cell division in $NKG2A^+$ CD8 T cells[32]. These results are also consistent with findings of elevated proliferative capacity of CD8 T cells in response to combined RT and dual NKG2A/PD-1 blockade[33].

Maximal efficacy of the full combination therapy relied on recruitment and activation of both CD8 and $CD4_{conv}$ T cells. While most previous publications examining NKG2A-targeted immunotherapy in pre-clinical cancer models have been focused on NK and CD8 T cells[7,8,34,35], to our knowledge, this is the first description of an anti-NKG2A blocking antibody interacting with both CD8 and $CD4_{conv}$ T cells to optimise its therapeutic benefits. Previous investigations identified a critical role of $CD4_{conv}$ T cells in helping CD8 T cells to achieve tumour rejection[36]. Indeed, it was reported that IL-2-producing CD4 helper T cells increased the number and cytolytic function of tumour-specific CD8 T cells[37]. Arina and colleagues also showed that adoptive transfer of alloantigen-specific CD4 T cells rescued exhausted neoantigen-specific CD8 T cells, leading to eradication of relapsing tumours[38]. To increase our understanding of the mechanisms behind cooperation between CD8 and CD4 T cells, the antibody-mediated depletion and Tocky timer system data provided insights into the dynamic contribution of T cells, including $CD4_{conv}$, in the TME, to the overall therapeutic effect following ATRi/RT/ImmuT combination. The impact of the double depletion of CD8/CD4 T cells on tumour growth, when compared with the depletion of CD8 T cells alone, correlates well with the data on accumulation of $CD4_{conv}$ T cells with new TCR activation in the tumour bed. Together, these data support the view that newly activated $CD4_{conv}$ T cells sustain effective antitumour immune responses in the TME by supporting more persistent CD8 T cell activity.

Our restimulation assay, using an HPV long-overlapping peptide, provides compelling evidence of an augmented level of antigen specificity that develops in mice following ATRi/RT and combination immune checkpoint blockade. An additional contributor to the effectiveness of our therapeutic approach could be its favourable impact on the intra-tumoral TCR repertoire. While the ATRi/RT combination alone exhibits a profound influence on the expansion of T cell clonotypes within the TME, our observations reveal a notable augmentation in the richness of the TCR repertoire and the emergence of numerous and large antigen-sharing TCR clusters in response to the ATRi/RT/ImmuT regimen. These findings collectively imply that the full combination is essential to achieving an optimised immune response against tumours due to its concomitant enhancement of TCR repertoire richness, clonality, and antigen specificity. In a pre-clinical breast cancer study, Rudqvist et al. reported that RT broadened the TCR repertoire and that combination of RT with anti-CTLA-4 antibody triggered T cell clone expansion and increased CDR3 clustering compared to control[39]. Moreover, differential response to anti-PD-L1 treatment has recently been attributed to variations in the TCR repertoire in a preclinical model of HNSCC[40]. Previously published human studies around TCR repertoire changes, secondary to immunotherapy or combination of immunotherapy and RT, have shown that increased TCR repertoire clonality and clustering are both correlated with response to immunotherapy and, therefore, desirable outcomes of combination therapeutic regimens[41–43]. In addition, Wand et al. documented heightened TCR diversity in the peripheral blood of responders among patients with HNSCC who underwent combined treatment involving cetuximab and nivolumab[44].

The ability of CD40 stimulation to support T cell antitumour responses has been extensively documented[45]. However, clinical development of CD40 agonist therapies have, so far, been significantly hindered by the occurrence of dose-limiting toxicities[46]. Our findings suggest that dual NKG2A/PD-L1 blocking intervention following ATRi/RT could mimic the efficacy of CD40 agonist therapy without recapitulating its significant and limiting toxicity. To add credibility to this hypothesis, our results show that anti-NKG2A/PD-L1 combination treatment following ATRi/RT increases the expression of CD40 on myeloid cells as well as CD40L on T cells, these two events subsequently mediating the recruitment, activation and proliferation of CD8 and $CD4_{conv}$ T cells in the TME. We show here that CD40/CD40L signalling is important in sustaining persistent TCR activation in CD8 T cells in response to ATRi/RT and immunotherapy combination. Meanwhile, our TCRseq analyses are in line with previous work describing an important function of this signalling pathway in affecting the TCR repertoire[47].

To conclude, in the present study, we unveil a means to redirect the full arsenal of T cell responses towards optimal cancer cell eradication in both HPV^- and HPV^+ tumours. This work provides a clear rationale for designing future clinical trials of radiation, DDRi and dual immune checkpoint blockade-based immunotherapy for patients with head and neck cancer.

Methods

Human single-cell RNA sequencing studies

Two single-cell RNA sequencing datasets from recently published studies[19,20] were analysed to explore immune cell types expressing *KLRC1/PDCD1* in head and neck squamous cell carcinomas (HNSCC). Both datasets include single-cell whole transcriptomes from HPV+ and HPV- HNSCC tumours and from peripheral blood; Cillo A et al. data also includes $CD45^+$ cells sorted from 5 tonsil tissues from independent patients without cancer. Gene/barcode matrices for each patient generated by CellRanger pipeline were downloaded from GSE164690 and GSE139324. Each dataset was processed separately in R using 'Seurat' package (v4.3.0). Cell-based and gene-based quality control filters were applied. Firstly, cells with less than 1000 transcripts (UMIs) or with less than 200 genes per cell were filtered out from further analysis. Next, cells that expressed more than 5000 genes or with ratio of mitochondrial transcripts higher than 10% per cell were also excluded. Finally, only genes expressed in at least two cells in each dataset were kept. Both datasets were than normalised using 'SCTransform' (with mitochondrial transcripts ratio effect regressed out), followed by dimensionality reduction and Louvain clustering. Cell-type cluster annotation was performed using sets of marker genes: CD3D with combination with CD4, CD8A and FOXP3 for $CD4^+$,

$CD8^+$ and regulatory T cells; KLRD1 and KIR2 for NK cells; CD19 and CD79A for B / plasma cells; CD14, CD68, FCGR3A and IL3RA for myeloid populations; TPSB2 and TPSAB1 for mast cells; EPCAM, KRT14 and KRT17 for epithelial cells; PECAM1 and RAMP2 for endothelial cells; COL1A1, COL1A2 and DCN for fibroblasts; RGS5 for pericytes. For the TCGA analyses, we downloaded clinical data and RSEM (RNAseq by Expectation-Maximamization) normalised expression data for the Head and Neck squamous cell carcinoma (HNSC) cohort of TCGA from the Firebrowse website [http://firebrowse.org/] version 2016012800.0.0. We generated the graphs using R package "ggplot". Statistic is Spearman R. We used R version 4.3.1.

Mouse models of head and neck cancer

All procedures involving animals were approved by the Animal Welfare and Ethical Review Board at the Institute of Cancer Research in accordance with Home Office Regulations under the Animals (Scientific Procedures) Act 1986. All animals were handled according to the Institute and U.K. Home Office guidelines and kept in specific pathogen-free facility and exposed to a 12-h light/dark cycle at constant temperature (22 ± 2 °C), with unrestricted access to food and water. Only female mice were used in the study to ensure reproducibility in tumour growth. In this study, we used models of murine immunocompetent HPV-negative head and neck cancer, MOC1 and MOC2 as well as HPV-positive head and neck cancer, mEER. We also used the HPV-positive murine immunocompetent model TC1. The C57BL/6 mouse cancer cell line MOC1 and MOC2 was kindly provided by Ravindra Uppaluri (Dana-Farber Cancer Institute). The C57BL/6 mouse cancer cell line mEER was kindly provided by Paola Vermeer (Sanford Research). The C57BL/6 mouse cancer cell line TC-1, a modified mouse lung epithelial cell line transformed with HPV-16 E6 and E7 and oncogenic HRAS, were a kind gift from Prof. Tzyy-Choou Wu (Johns Hopkins University, Baltimore, MD) and Prof. Eric Deutsch (Institut Gustave Roussy, Villejuif, France). Cells were cultured and maintained in Dulbecco Modified Eagle Serum (DMEM) supplemented with 10% foetal calf serum (FCS), 2mM L-glutamine, penicillin/streptomycin and sodium pyruvate. 6- to 14-week-old females C57BL/6 J WT (purchased from Charles River, stock 000664) or Nr4a3- Tocky: Foxp3- EGFP mice[25,48] were inoculated subcutaneously (ectopic) on the right flank with 4×10^6 cells for the MOC1 or 10^6 cells for the MOC2, mEER and TC1 models. In some experiments, mice were inoculated in the lip / cheek at the entrance of the oral cavity (orthotopic) with 3×10^6 MOC1 and 10^6 mEER cells. When indicated, cured animals were rechallenged subcutaneously 90 days after the first challenge. Mice were monitored daily for signs of distress or discomfort. The humane end-point was euthanasia by neck dislocation due to moribund status as determined by weight loss of 18% or more compared with maximum weight measured, inability to reach food or water, breathing difficulties, hunched intermittently, anorexia, dehydration, marked piloerection, lethargy and subdued. For the maximum tumour size allowance, according to Home Office guidelines, mice were euthanised by neck dislocation when the tumours reached 15 or 12 mm in one of the three dimensions for the ectopic or orthotopic models, respectively. We adhered to these size limits and guidelines in all experiments. Tumour growth was monitored twice a week using a calliper and expressed as volume ((length × width × depth)/2).

In vivo tumour treatments

In vivo treatments were initiated when tumours reached an average of 20–100 mm^3. Mice were randomised before treatment according to tumour sizes to obtain approximately same average tumour sizes between groups before the beginning of treatment regimens. The ATR inhibitor AZD6738 was provided by AstraZeneca and solubilised in 10% DMSO, 40% propylene glycol, 50% water, orally administrated 2 hours before irradiation for 4 consecutive days at 75 mg/kg/dose as indicated. Animal tumours were irradiated under anaesthesia with ketamine/xylazine injected intraperitoneally. Irradiation was initiated one day after ATR inhibitor dosing and was performed using an AGO 250 kV X-ray machine at a dose rate of 1.62 Gy/minute (AGO). Animals were irradiated in the prone position positioned underlead shielding with a 16-mm diameter aperture aligned over the Tumour. A total of 9 (RNAseq, flow cytometry and TCRseq experiments) to 18 Gy (survival experiments) radiation dose in three fractions were given. Radiation dose was measured using a Farmer Chamberand Unidos-E Dosemeter (both PTW). Three days after the last dose of radiotherapy, mice were treated with anti-NKG2A (200 μg/mouse i.v., every 4/5 days for two weeks for a total of three injections) and/or anti-PD-L1 antibodies (200 μg/mouse i.p., every ¾ days for two weeks for a total of 4 injections) provided by AstraZeneca. For the depletion of NK cells, mice were injected intraperitoneally with 200 μg/mouse of anti-NK1.1 antibody (BioXcell, clone PK136), twice weekly starting 1 day before treatment. For the depletion of CD8 T cells, mice were injected intraperitoneally with 200 μg/mouse of anti-CD8α (BioXcell, clone 2.43) twice weekly starting 1 day before treatment. For the depletion of CD4 T cells, mice were injected intraperitoneally with 500 μg/mouse of anti-CD4 (BioXcell or Biolegend, clone GK1.5) for the first injection starting 1 day before treatment and 250 μg/mouse twice weekly thereafter. For the analysis of cell cycle position, mice were injected i.p. with 1 mg of BrdU (BD Biosciences) 12 h before tumour harvest.

RNA sequencing

MOC1, MOC2 and mEER ectopic tumours were harvested 10 days after the last radiation dose. RNA from tumours was extracted and purified from tumours using the NucleoSpin RNA extraction kit (Qiagen). Library preparation and sequencing were performed by Genewiz (Leipzig, Germany). Library prep was strand-specific, used PolyA selection, with 2x150bp sequencing at 10 million pairs performed on an Illumina NovaSeq. Quality control was performed using FastQC. Low quality bases and adaptor sequences were removed using Trimmomatic. Reads were mapped to the M. musculus GRCm38 reference genome using HISAT2 and StringTie was used to generate gene count matrix for all samples. Differential gene expression was assessed using DESeq2. Active-subnetwork-orientated gene set enrichment analysis using STRING protein-protein interaction networks and Kyoto Encyclopedia of Genes and Genomes (KEGG) pathways was performed using pathfindR. Immune cell composition was estimated from transcriptomic data using mMCP-counter. Data visualisation utilised ggplot2 and ComplexHeatmap packages.

Flow cytometry analysis

Harvested tumours were excised, finely minced, and enzymatically digested for 30–45 min at 37 °C in PBS containing 1 mg/ml collagenase type VI (Sigma-Aldrich) 1 mg/ml DNase type I (Roche), 100 ng/ml Dispase (Sigma-Aldrich) and Trypsin. Digested tumours were smashed and filtered through 70 μm-pore cell strainers. Cells were centrifuged at 285 g at 4 °C for 10 min and pellets washed in PBS/2% FCS/5 mM EDTA. Harvested spleen were mechanically dissociated, smashed and filtered through 70 μm-pore cell strainers. Red blood cells were lysed by a 1 min incubation in ACK lysis buffer (Thermofisher Scientific). Cells were centrifuged at 285 *g* at 4 °C for 10 min and pellets washed in PBS/2% FCS. For some experiments, mice were bled 20 μL from the tail vein. PBMCs from human blood samples were isolated on a density gradient medium (Lymphoprep, STEMCELL Technologies). Cells were incubated 4 °C for 10 min with anti-mouse or anti-human CD16/CD32 (BD Pharmingen) prior to surface staining, 4 °C for 30 min. Dead cells were excluded using the Fixable Viability Dye eFluor™ 780 (Thermofisher Scientific). The complete list of antibodies used in this study can be found in the supplementary information (Table S1). Intranuclear detection of Ki67, FoxP3 and T-BET was performed using The Foxp3 Transcription Factor Staining Buffer Set (Thermofisher Scientific) following the manufacturer's instructions. For surface detection of

CD107a, cells were incubated in complete IMDM containing Golgi Plug/Golgi Stop (BD Biosciences) in the presence of a stimulation cocktail containing PMA and Ionomycin (Invitrogen) and mouse CD107a antibody for 4 h at 37 °C. Following surface antibody staining, cells were fixed using IC Fixation Buffer (Invitrogen), permeabilized in Permeabilization Buffer (Invitrogen), and stained with mouse IFN-γ antibody. Cell cycle position analyses were performed using the BD PharmigenTM BrDU Flow Kits (BD Biosciences) following the manufacturer's instructions. Samples were analysed on a LSR II or FACSymphony A5 (BD Biosciences) and FACS analyses were performed using the FlowJo version 10 software. Tocky timer data was analysed using the "TockyAnalysis" package in R (v 3.6.3). Gating strategies can de found in the supplementary information (Fig. S13).

Histology

For potential tumour-intended irradiation spillover to TDLN studies, mEER lip-bearing C57BL/6 mice were irradiated with 8 Gy with an underlead shielding positioned in the tumour site as previously described with or without a consecutive round of irradiation targeting the cervical lymph nodes in the neck area or left unirradiated. Lip tumours, TDLNs and sub-iliac LNs were collected 30 min after irradiation and fixed with 70% formalin overnight for histological analysis. Immunohistochemical staining for haematoxylin and eosin (H&E) and anti-mouse γ-H2AX (Ser139) antibody (Cell Signaling #9718, clone 20E3). Whole slide scanning was performed using Hamamatsu NanoZoomer S360 Digital Slide Scanner (HAMAMATSU PHOTONICS, UK) and visualised with QuPath 0.5.0 imaging analysis software.

TCR sequencing

TCR β-chain sequencing was performed by utilising whole RNA extracted from MOC1 tumour samples by using a quantitative experimental and computational TCR sequencing pipeline described previously [Oakes et al. Front Immunol, 2017]. Briefly, the TCR library preparation protocol consists of first a T4 ligation step to the 3′ end of the TCR cDNA which allows the amplification of all possible rearrangements using a single set of primers per locus and the incorporation of a UMI attached to each cDNA TCR molecule that enables correction for PCR and sequencing errors. The final library was prepared for sequencing according to the Illumina NovaSeq protocol immediately prior to loading. Sample was loaded at 1.2 pM with 15–20% of PhiX DNA at 1.8 pM. All samples were run in parallel, yielding 5 million reads per sample (2 × 150 bp paired end). The bioinformatic pipeline used for TCR identification, error correction and CDR3 extraction was Decombinator (freely available at https://github.com/innate2adaptive/Decombinator). For TCR analysis, clonality was calculated using the Gini coefficient.

$$Gini\ coefficient = \frac{\sum_{i=1}^{N}\sum_{j=1}^{N}|p_i - p_j|}{2N^2\bar{p}}$$

where p_i and p_j represents the frequency of the respective ith and jth sequences in the repertoire and $\bar{p}$ the average of the clone frequencies. Gini coefficient ranges from zero (maximal diversity of the repertoire or equal abundance of each sequence) to one, with high value representing extreme inequality (i.e. high clonality towards one sequence). Therefore, the Gini coefficient increases as the number of abundant clones rises, thus further reducing the frequency of less represented clones (i.e. higher inequality). Moreover, with increasing richness of repertoires, the inequality between dominant and subdominant (low frequency) clones gets wider, leading to a small rise in the Gini coefficient. This coefficient exhibits relatively lower sensitivity to undersample due to the exclusion of unique TCR sequences present in the total repertoire and consequently helps mitigate the inequality introduced by changes in frequency distribution. Unique productive clonotypes and clonality were compared across groups using One-way ANOVA with Dunnett's multiple comparisons tests. VJ genes junction circles and sample clonality plots were done using the VDJtools bioinformatic software[49]. Proportion occupied by quantile 1 across groups was compared using One-way ANOVA with Dunnett's multiple comparisons tests. For TCR clustering, the pairwise similarity between pairs of TCRs was measured on the basis of amino acid triplet sharing. Sharing was quantified using the normalised string kernel function stringdot (with parameters stringdot (type = 'spectrum', length = 3, normalised = TRUE) from the Kernlab package. The kernel is calculated as the number of amino acid triplets (sets of three consecutive amino acids) shared by two CDR3s, normalised by the number of triplets in each CDR3 being compared. The TCR similarity matrix was converted into a network diagram by using the iGraph package in R. Two TCRs were considered connected if the similarity index was >0.7. Per sample, we counted the number of clusters containing an expanded CDR3. An expanded CDR3 was considered if it was present above a threshold frequency of 2/1000 (corresponding to the top 1% of the empirical TCR frequency distribution). At this threshold, which we already described in previously published work [Barennes et al., 2020], the correlation between clonality and proportion of repertoire occupied by expanded TCRs is very strong and the number of TCRs labelled as expanded is greater than for higher thresholds for which this correlation is also significant, which enables to keep the greatest amount of data whilst still applying a stringent filtering step. To normalise the counts of clusters obtained for the input size, for each sample, we randomly selected, outside of the real clustering structure, the number of CDR3s equal to the number of expanded CDR3s in that sample and looked for clusters around those. A cluster was dominant if it was formed by more than 3 CDR3s.

Statistical methods

Statistical analyses were performed using GraphPad Prism software version 8, 9 and 10. Data are presented as means ± SEM and are from a single or cumulative of two to three independent experiments. Area under curves were used to determine statistical differences in tumour growth between groups. Statistical differences between survival groups were determined using the Log-rank Mantel Cox test. Intensity of marker expression was shown as geometric fluorescence mean intensity (MFI) in the positive population. Two-tailed unpaired *t* test or one-way ANOVA followed by Tuckey's post T-test were used for statistical analysis when two or multiple groups were analyzed, respectively. When data did not follow a Gaussian distribution, we used nonparametric Two-tailed Mann–Whitney *U* or Kruskal–Wallis tests followed by Dunn's post-*T* test for statistical analysis when two or multiple groups were analyzed, respectively. We used two-way ANOVA followed by Tuckey's multiple comparison test when two parameters were studied. Significant outliers were removed using Grubb's test.

Reporting summary

Further information on research design is available in the Nature Portfolio Reporting Summary linked to this article.

Data availability

Bulk RNA sequencing data and gene counts generated in this study have been deposited in the Gene Expression Omnibus (GEO) under accession number GSE267158. Raw bulk TCR sequencing data generated in this study have been deposited in the NCBI sequence read archive (SRA) under accession code PRJNA1132229 [http://www.ncbi.nlm.nih.gov/bioproject/1132229]. Additionally, TCR-β repertoires and the corresponding sample sheet are available from Figshare at https://doi.org/10.6084/m9.figshare.25795993.v1. Previously published human HNSCC single-cell RNAseq datasets used in this study are available through GEO with accession numbers GSE164690 and GSE139324. Normalised expression and clinical data for the TCGA Head and Neck squamous cell carcinoma (HNSC) cohort were

downloaded from the Firebrowse website [http://firebrowse.org/] version 2016012800.0.0. Source data are provided with this paper.

Code availability

Scripts used for the analysis of bulk RNAseq data generated in this study are available at https://github.com/mmclaughlin84/RNAseq_postalign_Rscripts. Code to reproduce public scRNAseq data processing and figures is available at https://doi.org/10.5281/zenodo.12686741. All software used in this study are publicly available and are described in the Methods section.

References

1. Burtness, B. et al. Pembrolizumab alone or with chemotherapy versus cetuximab with chemotherapy for recurrent or metastatic squamous cell carcinoma of the head and neck (KEYNOTE-048): a randomised, open-label, phase 3 study. *Lancet* **394**, 1915–1928 (2019).
2. Cohen, E. E. W. et al. Pembrolizumab versus methotrexate, docetaxel, or cetuximab for recurrent or metastatic head-and-neck squamous cell carcinoma (KEYNOTE-040): a randomised, open-label, phase 3 study. *Lancet* **393**, 156–167 (2019).
3. Ferris, R. L. et al. Phase II trial of post-operative radiotherapy with concurrent cisplatin plus panitumumab in patients with high-risk, resected head and neck cancer. *Ann. Oncol.* **27**, 2257–2262 (2016).
4. Lee, N. Y. et al. Avelumab plus standard-of-care chemoradiotherapy versus chemoradiotherapy alone in patients with locally advanced squamous cell carcinoma of the head and neck: a randomised, double-blind, placebo-controlled, multicentre, phase 3 trial. *Lancet Oncol.* **22**, 450–462 (2021).
5. Tao, Y. et al. Pembrolizumab versus cetuximab concurrent with radiotherapy in patients with locally advanced squamous cell carcinoma of head and neck unfit for cisplatin (GORTEC 2015-01 PembroRad): a multicenter, randomized, phase II trial. *Ann Oncol.* **34**, 101–110 (2023).
6. Wang, X., Xiong, H. & Ning, Z. Implications of NKG2A in immunity and immune-mediated diseases. *Front. Immunol.* **13**, 960852 (2022).
7. Andre, P. et al. Anti-NKG2A mAb Is a checkpoint inhibitor that promotes anti-tumor immunity by unleashing both T and NK cells. *Cell* **175**, 1731–1743.e1713 (2018).
8. van Montfoort, N. et al. NKG2A blockade potentiates CD8 T cell immunity induced by cancer vaccines. *Cell* **175**, 1744–1755 e1715 (2018).
9. Segal, N. H. et al. First-in-human dose escalation of monalizumab plus durvalumab, with expansion in patients with metastatic microsatellite-stable colorectal cancer. *J. Clin. Oncol.* **36** (2018).
10. Herbst, R. S. et al. COAST: an open-label, phase II, multidrug platform study of durvalumab alone or in combination with oleclumab or monalizumab in patients with unresectable, stage III non-small-cell lung cancer. *J. Clin. Oncol.* **40**, 3383–3393 (2022).
11. Cascone, T. et al. Neoadjuvant durvalumab alone or combined with novel immuno-oncology agents in resectable lung cancer: the phase 2 NeoCOAST platform trial. *Cancer Discov.* **13**, 2394–2411 (2023).
12. Galot, R. et al. A phase II study of monalizumab in patients with recurrent/metastatic squamous cell carcinoma of the head and neck: The I1 cohort of the EORTC-HNCG-1559 UPSTREAM trial. *Eur. J. Cancer* **158**, 17–26 (2021).
13. Karukonda, P., Odhiambo, D. & Mowery, Y. M. Pharmacologic inhibition of ataxia telangiectasia and Rad3-related (ATR) in the treatment of head and neck squamous cell carcinoma. *Mol. Carcinog.* **61**, 225–238 (2022).
14. Dillon, M. T. et al. ATR inhibition potentiates the radiation-induced inflammatory tumor microenvironment. *Clin. Cancer Res.* **25**, 3392–3403 (2019).
15. Patin, E. C. et al. Harnessing radiotherapy-induced NK-cell activity by combining DNA damage-response inhibition and immune checkpoint blockade. *J. Immunother. Cancer* **10**, e004306 (2022).
16. Vendetti, F. P. et al. ATR kinase inhibitor AZD6738 potentiates CD8+ T cell-dependent antitumor activity following radiation. *J. Clin. Invest.* **128**, 3926–3940 (2018).
17. Sheng, H. et al. ATR inhibitor AZD6738 enhances the antitumor activity of radiotherapy and immune checkpoint inhibitors by potentiating the tumor immune microenvironment in hepatocellular carcinoma. *J. Immunother. Cancer* **8**, e000340 (2020).
18. Vendetti, F. P. et al. The schedule of ATR inhibitor AZD6738 can potentiate or abolish antitumor immune responses to radiotherapy. *JCI Insight* **8**, e165615 (2023).
19. Kurten, C. H. L. et al. Investigating immune and non-immune cell interactions in head and neck tumors by single-cell RNA sequencing. *Nat. Commun.* **12**, 7338 (2021).
20. Cillo, A. R. et al. Immune landscape of viral- and carcinogen-driven head and neck cancer. *Immunity* **52**, 183–199 e189 (2020).
21. Judd, N. P. et al. ERK1/2 regulation of CD44 modulates oral cancer aggressiveness. *Cancer Res.* **72**, 365–374 (2012).
22. Williams, R. et al. Preclinical models of HPV+ and HPV- HNSCC in mice: an immune clearance of HPV+ HNSCC. *Head Neck* **31**, 911–918 (2009).
23. Hoover, A. C. et al. The role of human papillomavirus 16 E6 in anchorage-independent and invasive growth of mouse tonsil epithelium. *Arch. Otolaryngol. Head Neck Surg.* **133**, 495–502 (2007).
24. Bending, D. et al. A temporally dynamic Foxp3 autoregulatory transcriptional circuit controls the effector Treg programme. *EMBO J.* **37**, e99013 (2018).
25. Bending, D. et al. A timer for analyzing temporally dynamic changes in transcription during differentiation in vivo. *J. Cell Biol.* **217**, 2931–2950 (2018).
26. Hassan, J. et al. Single-cell level temporal profiling of tumour-reactive T cells under immune checkpoint blockade. *bioRxiv* https://doi.org/10.1101/2022.07.19.500582 (2022).
27. Altorki, N. K. et al. Neoadjuvant durvalumab with or without stereotactic body radiotherapy in patients with early-stage non-small-cell lung cancer: a single-centre, randomised phase 2 trial. *Lancet Oncol.* **22**, 824–835 (2021).
28. Antonia, S. J. et al. Durvalumab after chemoradiotherapy in stage III non-small-cell lung cancer. *N. Engl. J. Med.* **377**, 1919–1929 (2017).
29. West, H. et al. Atezolizumab in combination with carboplatin plus nab-paclitaxel chemotherapy compared with chemotherapy alone as first-line treatment for metastatic non-squamous non-small-cell lung cancer (IMpower130): a multicentre, randomised, open-label, phase 3 trial. *Lancet Oncol.* **20**, 924–937 (2019).
30. McBride, S. et al. Randomized phase II trial of nivolumab with stereotactic body radiotherapy versus nivolumab alone in metastatic head and neck squamous cell carcinoma. *J Clin Oncol* **39**, 30–37 (2021).
31. Salome, B. et al. NKG2A and HLA-E define an alternative immune checkpoint axis in bladder cancer. *Cancer Cell* **40**, 1027–1043 e1029 (2022).
32. Borst, L. et al. NKG2A is a late immune checkpoint on CD8 T cells and marks repeated stimulation and cell division. *Int. J. Cancer* **150**, 688–704 (2022).
33. Battaglia, N. G. et al. Combination of NKG2A and PD-1 blockade improves radiotherapy response in radioresistant tumors. *J. Immunol.* **209**, 629–640 (2022).
34. Ruggeri, L. et al. Effects of anti-NKG2A antibody administration on leukemia and normal hematopoietic cells. *Haematologica* **101**, 626–633 (2016).
35. Kamiya, T., Seow, S. V., Wong, D., Robinson, M. & Campana, D. Blocking expression of inhibitory receptor NKG2A overcomes tumor resistance to NK cells. *J. Clin. Invest.* **129**, 2094–2106 (2019).

36. Poncette, L., Bluhm, J. & Blankenstein, T. The role of CD4 T cells in rejection of solid tumors. *Curr. Opin. Immunol.* **74**, 18–24 (2022).
37. Bos, R. & Sherman, L. A. CD4+ T-cell help in the tumor milieu is required for recruitment and cytolytic function of CD8+ T lymphocytes. *Cancer Res.* **70**, 8368–8377 (2010).
38. Arina, A. et al. Transfer of allogeneic CD4+ T cells rescues CD8+ T cells in anti-PD-L1-resistant tumors leading to tumor eradication. *Cancer Immunol. Res.* **5**, 127–136 (2017).
39. Rudqvist, N. P. et al. Radiotherapy and CTLA-4 blockade shape the TCR repertoire of tumor-infiltrating T cells. *Cancer Immunol. Res.* **6**, 139–150 (2018).
40. John, J. et al. Divergent outcomes of anti-PD-L1 treatment coupled with host-intrinsic differences in TCR repertoire and distinct T cell activation states in responding versus non-responding tumors. *Front. Immunol.* **13**, 992630 (2022).
41. Au, L. et al. Determinants of anti-PD-1 response and resistance in clear cell renal cell carcinoma. *Cancer Cell* **39**, 1497–1518 e1411 (2021).
42. Formenti, S. C. et al. Radiotherapy induces responses of lung cancer to CTLA-4 blockade. *Nat. Med.* **24**, 1845–1851 (2018).
43. Valpione, S. et al. The T cell receptor repertoire of tumor infiltrating T cells is predictive and prognostic for cancer survival. *Nat. Commun.* **12**, 4098 (2021).
44. Wang, X. et al. T cell repertoire in peripheral blood as a potential biomarker for predicting response to concurrent cetuximab and nivolumab in head and neck squamous cell carcinoma. *J. Immunother. Cancer* **10**, e004512 (2022).
45. Bullock, T. N. J. CD40 stimulation as a molecular adjuvant for cancer vaccines and other immunotherapies. *Cell Mol. Immunol.* **19**, 14–22 (2022).
46. Bates, K. M. et al. Spatial characterization and quantification of CD40 expression across cancer types. *BMC Cancer* **23**, 220 (2023).
47. Fahnrich, A. et al. CD154 costimulation shifts the local T-cell receptor repertoire not only during thymic selection but also during peripheral T-dependent humoral immune responses. *Front Immunol* **9**, 1019 (2018).
48. Bozhanova, G. et al. CD4 T cell dynamics shape the immune response to combination oncolytic herpes virus and BRAF inhibitor therapy for melanoma. *J. Immunother. Cancer* **10**, e004410 (2022).
49. Shugay, M. et al. VDJtools: unifying post-analysis of T cell receptor repertoires. *PLoS Comput. Biol.* **11**, e1004503 (2015).

Acknowledgements

This work was supported by Cancer Research UK (C7224/A23275; DRCRPG-Nov22/10008; C7224/A28724), the Oracle Cancer Trust (ORC 22-ICR0920), the Rosetress Trust (CM48 and CM444), and the RM/ICR NIHR Biomedical Research Centre (IS-BRC-1215-20021). We would like to acknowledge Harriet Whittock, Mark Allen and Peter John-Baptiste for mice monitoring.

Author contributions

E.C.P., K.J.H., A.A.M., A.R., M.M., E.C., S.A.S., and P.N. contributed to the conception and design of the research as well as in writing the manuscript; E.C.P., P.N., C.C.W.H., M.M., M.T.D., L.G., S.F., H.B., J.G., V.R., J.K., A.M., L.H., M.P., and A.R. performed the experiments and acquired data; E.C.P., K.J.H., M.M., M.T.D., P.N., J.G., S.A.S., M.P., A.A.M., A.P. and M.O. contributed to the analysis and interpretation of the data. A.R., P.N., M.M., A.P., and CCWH provided support for bioinformatics analysis; M.T.D., P.N., H.S., J.P.B., J.M., and L.G. contributed to the collection and supply of clinical samples. E.C. and S.A.S. contributed to the supply of reagents. M.O. contributed to the supply of Tocky mice. K.J.H. is the guarantor, senior author and provided funding for the project. All authors read and approved the final manuscript.

Competing interests

E.C. and S.A.S. are employees and stockholders of AstraZeneca. The remaining authors declare no competing interests.

Additional information

Supplementary information The online version contains supplementary material available at https://doi.org/10.1038/s41467-024-51236-6.

Correspondence and requests for materials should be addressed to Emmanuel C. Patin.

Peer review information *Nature Communications* thanks the anonymous reviewer(s) for their contribution to the peer review of this work. A peer review file is available.